Acidic processing of mineral dust iron by anthropogenic compounds over the north Pacific Ocean.

F. Solmon, P.Y. Chuang, N. Meskhidze, Y. Chen

Acidic processing of mineral dust iron by anthropogenic compounds over the north Pacific Ocean

F. Solmon,[1] P. Y. Chuang,[2] N. Meskhidze,[3] and Y. Chen[4]

Received 14 May 2008; revised 18 September 2008; accepted 23 October 2008; published 24 January 2009.

[1] Atmospheric processing of mineral aerosol by anthropogenic pollutants may be an important process by which insoluble iron can be transformed into soluble forms and become available to oceanic biota. Observations of the soluble iron fraction in atmospheric aerosol exhibit large variability, which is poorly represented in models. In this study, we implemented a dust iron dissolution scheme in a global chemistry transport model (GEOS-Chem). The model is applied over the North Pacific Ocean during April 2001, a period when concentrations of dust and pollution within the east Asia outflow were high. Simulated fields of many key chemical constituents compare reasonably well with available observations, although some discrepancies are identified and discussed. In our simulations, the production of soluble iron varies temporally and regionally depending on pollution-to-dust ratio, primarily due to strong buffering by calcite. Overall, we show that the chemical processing mechanism produces significant amounts of dissolved iron reaching and being deposited in remote regions of the Pacific basin, with some seasonal variability. Simulated enhancements in particulate soluble iron fraction range from 0.5% to 6%, which is consistent with the observations. According to our simulations, ~30% to 70% of particulate soluble iron over the North Pacific Ocean basin can be attributed to atmospheric processing. On the basis of April 2001 monthly simulations, sensitivity tests suggest that doubling SO_2 emissions can induce a significant increase (13% on average, up to 40% during specific events) in dissolved iron production and deposition to the remote Pacific. We roughly estimate that half of the primary productivity induced by iron deposition in a north Pacific high-nutrient low-chlorophyll region is due to soluble iron derived from anthropogenic chemical processing of Asian aerosol.

Citation: Solmon, F., P. Y. Chuang, N. Meskhidze, and Y. Chen (2009), Acidic processing of mineral dust iron by anthropogenic compounds over the north Pacific Ocean, *J. Geophys. Res.*, *114*, D02305, doi:10.1029/2008JD010417.

1. Introduction

[2] Iron (Fe) has been identified as a limiting factor for phytoplankton growth in high-nutrient low-chlorophyll (HNLC) regions of the ocean. By modulating CO_2 uptake in these regions, it is believed that iron may influence primary productivity and hence the global carbon cycle and climate [*Jickells et al.*, 2005; *Martin*, 1990]. In the remote ocean, atmospheric deposition of dust particulate matter is thought to be the major process by which iron can be supplied to ecosystems [*Cassar et al.*, 2007; *Bonnet and Guieu*, 2004; *Sarthou et al.*, 2003], though recent studies outline also the importance of iron supply by upwelling deep water [*Blain et al.*, 2007; *Meskhidze et al.*, 2007]. In the atmosphere, iron can be found and transported in a variety of chemical forms, both water-soluble and -insoluble. It is generally believed that only the soluble fraction of iron can be considered as bioavailable for phytoplankton [*Baker et al.*, 2006; *Jickells et al.*, 2005; *Achilles et al.*, 2003].

[3] Measurements of the dissolved iron fraction (DIF, defined as the fraction of the total iron that is water soluble; we use this terminology to be consistent with previous studies. However, it would be more accurate to use the term "soluble iron fraction" because the iron need not be in the aqueous state (as implied by "dissolved") in the atmosphere in order to be bioavailable) in crustal material collected in source regions generally report very low values of solubility [*Bonnet and Guieu*, 2004]. However, numerous experimental studies, based on different analytical techniques, have shown that aerosol DIF can increase during atmospheric transport and is characterized by large variability (0.01 to 80% [*Mahowald et al.*, 2005; *Baker et al.*, 2006; *Chen*, 2005]). This variability is a source of significant uncertainty in our understanding of the impact of iron to marine ecosystems and biogeochemical cycles [*Blain et al.*, 2008]. In global climate modeling, DIF is often prescribed

[1] Laboratoire d'Aérologie, UPS-CNRS, Toulouse, France.
[2] Earth and Planetary Sciences Department, University of California, Santa Cruz, California, USA.
[3] Department of Marine, Earth and Atmospheric Sciences, North Carolina State University, Raleigh, North Carolina, USA.
[4] Trinity Consultants, Irvine, California, USA.

0148-0227/09/2008JD010417

as constant over the globe [*Archer and Johnson*, 2000; *Fung et al.*, 2000; *Gao et al.*, 2003; *Aumont et al.*, 2008; *Jin et al.*, 2007].

[4] On the basis of laboratory evidence, several mechanisms have been proposed as factors leading to an increase of DIF during dust atmospheric transport of mineral dust. For example, photo-reductive processes promoted by oxalate or other organic substances [*Pehkonen et al.*, 1993], in-cloud processing [*Desboeufs et al.*, 2001], and acidic attack by anthropogenic compounds [*Zhuang et al.*, 1992; *Zhu et al.*, 1993; *Spokes and Jickells*, 1996; *Meskhidze et al.*, 2003; *Boyle et al.*, 2005]. However, because of the complexity of aerosol-phase iron chemistry, dissolution mechanisms and the limited amount of field data available to constrain models, there is still no clear consensus regarding the importance of these mechanisms in DIF evolution. For example, *Luo et al.* [2005] concluded than in-cloud processing was a dominant factor for iron dissolution whereas *Fan et al.* [2006] concluded that the coating of dust particles by sulfate from ambient trace gas deposition was likely the main factor for the enhanced fertilization of the modern northern hemisphere ocean. Despite the difficulty of atmospheric iron cycle modeling, 3D models are needed as a framework to understand the global budget and cycling of iron. An effort is being made to improve the representation of DIF evolution in global models according to these mechanisms [*Luo et al.*, 2005; *Fan et al.*, 2006], although parameterizations used to describe the DIF evolution in global modeling studies are generally simplified due to the computational expense of introducing complete mechanisms.

[5] Recently, *Meskhidze et al.* [2005] (hereafter referred to as M05) developed an extensive mechanism to describe dust iron processing by anthropogenic pollutants and applied it to study the east Asia outflow. The scheme relies upon a description of dust heterogeneous chemistry, deliquesced particle pH evolution and mineral dissolution to predict the evolution of the DIF under different ambient conditions. In M05, this chemical scheme is coupled to a Lagrangian box model, and is used to study important mechanisms determining iron solubilization during specific dust events over the North Pacific Ocean.

[6] In the present study, we extend this approach by introducing the M05 parametrization into the GEOS-Chem 3D global chemistry transport model [*Bey et al.*, 2001a; *Park et al.*, 2004; *Fairlie et al.*, 2007]. The overall goal of this study is primarily to better describe and quantify the impact of anthropogenic activities on atmospheric Fe cycling at the ocean basin scale and identify regions where dust-pollution interactions may play a major role. One of our longer term goals is to assess the potential impact of future anthropogenic activity on iron cycle and ocean fertilization.

[7] We focus this study on the north Pacific basin due to the coexistence of dust and pollution as part of the east Asia outflow, and because the remote north Pacific and particularly the subartic Aleutian and equatorial Pacific regions are identified as two main HNLC regions of the globe [*Jin et al.*, 2007; *Duce and Tindale*, 1991]. After a description of the coupled scheme implementation, we will focus on results from this model over the north Pacific Ocean (NPO) domain during year 2001, during which many detailed in situ measurements are available as described below.

2. Model Description

2.1. Geos-Chem Chemistry Transport Model

[8] GEOS-Chem is a global chemistry transport model driven by GEOS assimilated meteorological fields from the NASA GMAO. The year 2001 GEOS-3 meteorological fields used are initially at 1° resolution and degraded to $2 \times 2.5°$ horizontal resolution for input to the GEOS-Chem standard configuration used in this study. The model has 48 sigma levels from the surface to approximately 0.01 hPa. In its full chemistry configuration, GEOS-Chem includes H_2SO_4-HNO_3-NH_3 aerosol thermodynamics coupled to an O_3-NO_x-hydrocarbon-aerosol chemical mechanism [*Bey et al.*, 2001a, 2001b; *Park et al.*, 2004]. Sulfur compounds, carbonaceous aerosols and sea-salt emission and chemistry are accounted for and described by *Park et al.* [2004], *Heald et al.* [2006b] and *Alexander et al.* [2005]. GEOS-Chem simulates aerosol mass concentrations and does not include aerosol microphysics. Of particular relevance to this study, the dust mobilization and transport scheme is described in detail by *Fairlie et al.* [2007].

2.2. "Dust and Anthropogenic Modes" Definition and Chemical Processes

[9] GEOS-Chem predicts dust emission and concentration distributed in 4 standard bins with diameter bin boundaries of 0.2, 2.0, 3.2, 6.0 and 12 μm [*Fairlie et al.*, 2007]. Theoretically, the iron chemistry should be treated for every size resolved bin. However, in order to reduce the number of transported tracers, we did not treat chemical processes explicitly for each of the standard bins. Instead, we defined a "dust mode" in which all the important new species in the iron scheme (described in section 2.2.2) can be emitted, formed, transported and removed. In any grid cell and at any time, the dust mode size properties are calculated from the standard bins: the dust mode mass concentration is equal to the sum of individual dust bin concentrations, and the dust mode effective radius, settling and dry deposition velocities are calculated as mass weighted averages of the individual standard bin effective radii, settling and dry deposition velocities. This way, sedimentation and dry deposition of the new mineral species (described in section 2.2.2) transported and formed in the dust mode account for the size distribution of dust particle during transport from sources to remote areas. The wet removal of mineral species belonging to the dust mode is treated the same way as for standard dust bins and depends only on species concentrations and rainfall rates [*Liu et al.*, 2001].

[10] In addition to the above-defined dust mode, we define an "anthropogenic mode" to designate aerosol species (sulfate–nitrate–ammonia) that are treated by the standard GEOS-Chem but which are not associated to dust particles. As described below, the interactions between the dust and anthropogenic modes can occur via gas phase only, since coagulation processes are not accounted for in the model.

[11] The calculation of mineral dissolution and dissolved iron formation occurs in the dust mode and includes the following important steps: (1) the definition of an initial mineral composition characterizing dust at the source region;

Table 1. Initial Mineral Composition Assumed for the Dust Mode[a]

Dust Mode Mineral Content	Initial Conditions for Model Simulation (%wt.)
Gypsum ($CaSO_4$)	6
Calcite ($CaCO_3$)	11
Albite ($NaAlSi_3O_8$)	17
Microcline ($KAlSi_3O_8$)	8
Illite ($K_{0.6}Al_{2.3}Mg_{0.25}Si_{3.5}O_{10}(OH)_2$)	20
Smetcite/Montmorillonite ($Na_{0.6}Al_{1.4}Mg_{0.6}Si_4(OH)_2.4H_2O$)	8
Hematite (Fe_2O_3)	5
Quartz (SiO_2)	20
Kaolinite ($Al_2Si_2(OH)_5$)	5

[a]See the study by *Meskhidze et al.* [2005] for details.

(2) the heterogeneous uptake of water and soluble gases by dust resulting in a liquid coating around the dust particle; (3) the dissolution of dust minerals in this solution, depending strongly on solution pH and ambient temperature; and (4) the thermodynamic equilibrium and chemical speciation of the dissolved minerals in the solution. We will give here a description of some key aspects of the M05 scheme coupled to the 3D Eulerian GEOS-Chem model.

2.2.1. Dust Mineral Composition

[12] The dust mineral composition is representative of Gobi desert mineralogy and considers nine minerals listed in Table 1. Given our primary interest in the north Pacific region, this simplification is not unreasonable. Hematite is assumed to be the only source for dissolved iron, despite the fact that a fraction of iron can be found in other minerals [*Coey*, 1988] and especially clays [*Journet et al.*, 2008]. However, because of the great variability of iron content in clays, as well as the lack of related spatial distribution data, we maintain here the initial mineral composition of M05 and assume hematite is the only source of iron. As the dissolution kinetics of most of these minerals is slow, we assume that their mass fraction remains constant during transport, and their concentration is determined by the dust mode concentration and initial composition. The exceptions are calcite and gypsum, whose concentrations can vary significantly during transport due to fast dissolution and precipitation kinetics. These species are therefore represented by specific tracers in this scheme. Finally, we do not consider quartz dissolution since it does not affect solution pH.

2.2.2. Dissolved Species Simulated by the Model

[13] Ten tracers representing dissolved species transported as part of the dust mode have been added to the standard GEOS-Chem scheme (Table 2). As discussed below, the concentration of these species are determined by heterogeneous uptake of gas by dust and mineral dissolution.

2.2.2.1. Dust Mode Sulfate-Nitrate-Ammonium

[14] Sulfate is produced in the dust mode (dust-SO_4) as a result of the immediate condensation of gas phase sulfuric acid (calculated by the GEOS-Chem sulfate scheme) and the direct absorption of SO_2 by dust leading to production of aqueous sulfate (equation (1)).

$$\frac{d[dust-\mathrm{SO_4}]}{dt}=\frac{d[\mathrm{H_2SO_4}]_g}{dt}\cdot\left[\frac{S_d}{S_d+S_a}\right]+k_G\cdot[dust]\cdot[\mathrm{SO_2}] \quad (1)$$

[15] The amount of H_2SO_4 deposited on the dust and anthropogenic modes is determined by surface area. The dust mode effective surface area S_d is determined as the sum of individual dust bin surface areas which are calculated from local standard bin mass concentrations and diameters. S_a represents the anthropogenic mode surface area, calculated from the anthropogenic mode sulfate concentration assuming an effective diameter of 0.12 μm, following M05. The simplified heterogeneous absorption depends on dust mode concentration [*dust*], SO_2 concentration and a bulk uptake coefficient $k_G = 9 \times 10^{-8}$ $m^3 \mu g^{-1} s^{-1}$ [*Herring et al.*, 1996]. To insure mass conservation and interactivity in GEOS-Chem, SO_2 and anthropogenic sulfate aerosol concentrations are depleted according to the different terms of dust-SO_4 production.

[16] Once in solution, dust-SO_4 can initiate a number of aqueous chemical reactions. At the early stage of dust transport, one of the most important reactions is dissolution of calcium carbonate ($CaCO_3$) and subsequent formation of gypsum $CaSO_4$. During long-range transport of mineral dust, $CaSO_4$ becomes oversaturated and eventually precipitates out from the solution, in agreement with most experimental data [*Zhou and Tazaki*, 1996; *Mori et al.*, 1998; *Böke et al.*, 1999; *Kim and Park*, 2001]. This mechanism is central to the dust pH buffering effects as illustrated in the next sections. Sulfate speciation and its effect on dust pH are calculated using the thermodynamic module ISORROPIA [*Nenes et al.*, 1998; *Park et al.*, 2004].

[17] Sources of the dust mode nitrate (dust-NO_3) in the model are gas-phase HNO_3 condensation to dust mode particles and direct absorption of NO_2 gas, determined by a bulk uptake coefficient (equation (2)).

$$\frac{d[dust-\mathrm{NO_3}]}{dt}=k_{G2}\cdot[dust]\cdot[\mathrm{NO_2}]+S_{eq} \quad (2)$$

Table 2. Dissolved Species Associated to the Dust Mode and Introduced in GEOS-Chem as New Tracers and Corresponding Chemical Forms Allowed[a]

Tracer Symbol	Transported Chemical Forms	Local Chemical Speciation
Dust-SO_4	$[SO_4^{2-}]_{aq} + [HSO_4^{2-}]_{aq}$	$[FeSO_4^+]_{aq}$, $[AlSO_4^+]_{aq}$, $[Na_2SO_4]_s$, $[NaHSO_4]_s$, $[(NH_4)_2SO_4]_s$, $[NH_4HSO_4]_s$, $[(NH_4)_3H(SO_4)_2]_s$, $[CaSO_4]_s$
Dust-NO_3	$[NO_3^-]_{aq}$	$[NH_4NO_3]_s$, $[NaNO_3]_s$
Dust-NH_4	$[NH_4^+]_{aq}$	$[(NH_4)_2SO_4]_s$, $[NH_4HSO_4]_s$, $[(NH_4)_3H(SO_4)_2]_s$, $[NH_4NO_3]_s$
Dust-Na	$[Na^+]_{aq}$,	$[NaNO_3]_s$, $[NaHSO_4]_s$, $[Na_2SO_4]_s$
Dust-Al	$[Al^{3+}]_{aq}$,	$[Al(OH)^{2+}]_{aq}$, $[Al(OH)_2^+]_{aq}$, $[Al(OH)_3^0]_{aq}$, $[Al(OH)_4^-]_{aq}$, $[AlSO_4^+]_{aq}$, $[Al(OH)_3]_s$
Dust-Fe_d	$[Fe^{3+}]_{aq}$,	$[Fe(OH)^{2+}]_{aq}$, $[Fe(OH)_2^+]_{aq}$, $[Fe(OH)_3^0]_{aq}$, $[Fe(OH)_4^-]_{aq}$, $[FeSO_4^+]_{aq}$, $[Fe(OH)_3]_s$
Dust-K	$[K^+]_{aq}$,	
Dust-Mg	$[Mg^{2+}]_{aq}$	
Dust-Sil	$[H_4SiO_4^0]_{aq}$	
Dust-Ca^{2+}	$[Ca^{2+}]_{aq}$	
Dust-$CaCO_3$	$[CaCO_3]_s$	
Dust-$CaSO_4$	$[CaSO_4]_s$	

[a]The local speciation is done using ISORROPIA completed by specific chemical mechanisms developed in the study by *Meskhidze et al.* [2005] (see text).

where $k_{G2} = 1 \times 10^{-7}$ $m^3 \mu g^{-1} s^{-1}$ [*Herring et al.*, 1996]. Depending on aerosol chemical composition, S_{eq} represents either the rate of condensation of gas-phase HNO_3 to the dust mode deliquesced solution or the volatilization of dissolved nitrate from the dust mode solution. We suppose here that the mass exchange between the gas and aerosol is fast compared to the model chemical time step (30 min) and that S_{eq} can thus be reasonably determined considering thermodynamic equilibrium between gas phase precursors and dissolved compounds in the coating solution. The thermodynamic module ISORROPIA, which treats the system water-ammonia-sulfate-nitrate-chloride-sodium system, is used for this purpose. In order to account for possible transfer of mass between the anthropogenic mode and the dust mode via the gas phase, ISORROPIA is run iteratively for each mode until stable gas phase concentrations are obtained.

[18] On the same principle, the dust mode ammonium (dust-NH_4) is determined only via gas NH_3 phase condensation/evaporation driven by thermodynamic equilibrium. Following M05, we did not consider at this stage chlorine compounds in the system.

2.2.2.2. Dust Mode Mineral Cations

[19] $CaCO_3$ dissolution/precipitation is one of the major controls of mineral aerosol solution pH. Calcite dissolution is treated explicitly as a kinetic process depending on pH and temperature of the dust coating solution.

$$\frac{d[dust - \mathrm{Ca}]}{dt} = W_{Ca/cal}.[dust] \cdot R_{Ca} - S_{Ca/CaSO_4} \quad (3)$$

Where $W_{Ca/cal}$ is the fraction of Ca in calcite and R_{ca} is the dissolution rate of calcite given by:

$$R_{ca} = K_r(T).a(H^+)^m.f(\Delta G_r).A.W \quad (4)$$

R_{ca} has units of moles of calcite dissolved per gram of dust per second, K_r has units of mole dissolved/m^2 of calcite/s and is a function of temperature, T, $a(H^+)$ is the H^+ activity (linked to pH), $m = 1$ is an empirical parameter, f is a function of Gibbs free energy, ΔG_r, and accounts for the variation of the rate with deviation from equilibrium, $A = 0.1$ is the specific surface area of mineral in units of m^2/g of calcite, and $W = 11$ is the weight fraction of the calcite in dust in units of g of mineral/g of dust.

[20] As mentioned above, $CaSO_4$ dissolution is not considered as a source of calcium cations in view of evidence that gypsum precipitates in mineral aerosol during long-range transport. Finally in equation (3), $S_{Ca/CaSO4}$ represents a sink term due to precipitation of $CaSO_4$ which is determined by equilibrium thermodynamic process described in M05. When precipitation occurs, dust-Ca^{2+} with equivalent molar amount of sulfate is removed from the solution.

[21] The remainder of the dust-mode mineral cations (Table 2) results from the pH- and temperature-dependant dissolution kinetics of different dust minerals summarized in Table 1. Dissolution follows the same formulation as equation (4) and specific rate constants are detailed in M05. All cations are first converted to equivalent molar concentration of sodium before entering aqueous-phase equilibrium reactions in ISORROPIA for speciation and pH determination. As discussed in M05, such simplification should not lead to significant errors in production of dissolved Fe. Nevertheless, the new version of ISORROPIA (ISORROPIA II [*Fountoukis and Nenes*, 2007]) that explicitly accounts for calcium and other mineral cations chemistry will be implemented in future and may represent an improvement for the present dust-iron chemistry scheme.

2.2.2.3. Dust Mode Dissolved Iron

[22] In our approach, dust mode dissolved iron (dust-Fe_d) results exclusively from the initial content of dissolved iron associated with dust particles and hematite dissolution during transport.

[23] We fixed the dust initial DIF (i.e., at the emission source) to be 0.45 %. This value is the average measured DIF in a dust source region in Dunhuang, China during the ACE-Asia campaign [*Chuang et al.*, 2005]. For reference, measured values ranged from 0.05 to 1% and we chose the mean value of 0.45%. The effect of changing initial DIF is discussed in section 4.

[24] Hematite dissolution follows a formulation similar to equation (4) (see M05 for full details) but a more complex three-stage kinetic process is considered for specification of dissolution constant (K_r). The first stage, which is characterized by relatively slow dissolution, is applicable to the dissolution of the first 0.8% of the oxide's mass; the second stage, with an accelerated dissolution rate likely associated with the digestion of the oxide phase [*Gorichev et al.*, 1976] is applied when the mass of oxide dissolution ranges from 0.8 to 40%; and the third stage is applied when the dissolved mass is >40%, as dissolution approaches completion [*Azuma and Kametani*, 1964].

[25] The acid dissolution of Fe from hematite produces dissolved iron initially in a +III oxidation state. Once in solution, Fe(III) can be speciated in different complexes according to solution pH (see Table 2), including an amorphous phase.

[26] Subsequent photoreduction cycling in solution (FeIII/FeII) has been shown experimentally [*Pehkonen et al.*, 1993; *Siefert et al.*, 1994] but is not accounted for in the model. As discussed in M05, this cycling is not likely to modify the total amount of dissolved iron, as long as the solution remains undersaturated with regards to Fe(III), which is most often the case.

[27] Dissolved Fe(II) can, however, be directly produced from the solid phase and enter the solution phase via photo-induced reductive dissolution processes, possibly promoted by organic photo-sensitizers (e.g., oxalate, formate and other humic species) currently found in aerosols and cloud droplets [*Pehkonen et al.*, 1993; *Siefert et al.*, 1994; *Warneck*, 2000]. These processes are not considered in the present study and would require further model development. Their potential impacts on iron dissolution enhancement have been discussed through sensitivity studies in M05.

[28] Finally, in the present study, the possibility of dissolved iron carried by the anthropogenic mode has not been considered. As discussed below, this source of iron, which has been linked to combustion activities, could be significant in the vicinity of industrialized regions [*Chuang et al.*, 2005; *Luo et al.*, 2008].

3. Iron Processing on the North Pacific During April 2001

[29] Aerosol concentration, chemical composition and transport for the East Asian continental outflow has been

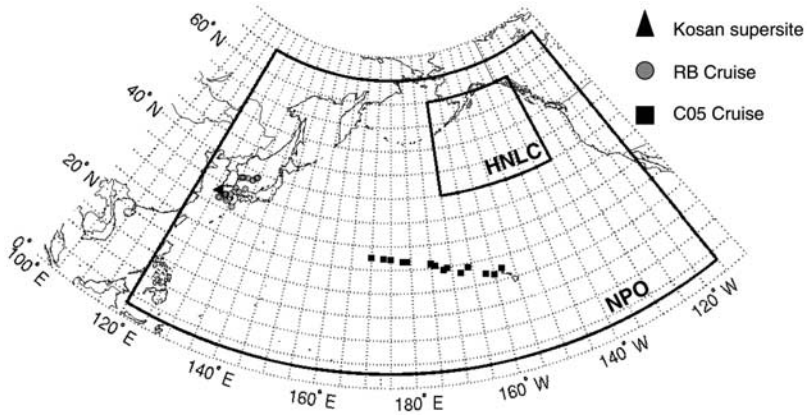

Figure 1. Overview of the domain of interest and geographical location corresponding to the different data sets collected during April 2001 and used in this study. The two delimited area NPO and HNLC are used to perform regional budgets (see text).

previously studied by a number of investigators, notably during the TRACE-P and ACE-Asia field campaigns [*Jacob et al.*, 2003; *Huebert et al.*, 2003] and from studies combining modeling [*Carmichael et al.*, 2001; *Zhang and Carmichael*, 1999] and remote sensing [*Kim et al.*, 2007]. The GEOS-Chem model has also been extensively evaluated over this domain, focusing on ozone chemistry [*Bey et al.*, 2001b], anthropogenic aerosols [*Park et al.*, 2004; *Heald et al.*, 2006a, 2006b] and dust aerosol [*Fairlie et al.*, 2007]. Model simulations for the chemical evolution of mineral iron in dust plumes advected over the NPO have also been performed [*Meskhidze et al.*, 2005]. In this section, we will present GEOS-Chem simulation results performed in full aerosol-chemistry mode including the new dust chemistry scheme described above. The simulations focus on 1–30 April 2001 and incorporate a 15-day spin-up time from 15 March to 1 April.

[30] GEOS-Chem simulations for trans-Pacific transport of dust and pollution for April 2001 period have being extensively validated by *Heald et al.* [2006a] using ground-based data as well as satellite aerosol optical depth (AOD) and CO retrievals. In the present study, we will focus on newly introduced variables affecting Fe dissolution.

3.1. Simulation and Evaluation of the Dust Heterogeneous Chemistry

[31] The iron dissolution scheme described in section 2 relies upon a number of hypotheses regarding dust mineral composition and heterogeneous chemistry processes. To evaluate the realism of the scheme, it is first necessary to evaluate key variables determining dissolved iron production during the dust transport. These variables are (1) the total iron content carried by dust and (2) the concentration of major dissolved ions which determine the pH of deliquesced mineral dust particles. We compare simulated results to surface measurements collected during April 2001 over the NPO domain (Figure 1) as part of the ACE-Asia campaign. We use data from the Kosan (sometimes Gosan) supersite located on Cheju (sometimes Jeju) island, South Korea, which is frequently situated in the outflow of continental east Asia, as well as data from the R/V Ron Brown cruise which sampled the western Pacific region, primarily in the Yellow Sea and Sea of Japan. For data farther east in the NPO region, we also considered another set of shipboard measurements collected primarily west of Hawaii during April 2001 [*Chen*, 2005, referred to hereafter as C05].

3.1.1. Total Iron

[32] *Heald et al.* [2006a] and *Fairlie et al.* [2007] show that the GEOS-Chem dust module is able to reproduce the timing and location of dust outbreaks during the ACE-Asia period. Figure 2a shows that the intense outbreak of 10 April over the Kosan site is reasonably reproduced by the model. Measured aerosol size distributions from the Kosan site during large dust breaks exhibits a lognormal mass distribution centered on 5 μm diameter, indicating that most of the dust mass should be accounted for by the model since it has a maximum size of 12 μm diameter. However, part of the underestimation of simulated dust concentration (Figure 2a), notably during lower amplitude dust events (19–26 April), could be due to a significant fraction of the mass transported by the particles larger than this maximum size. Uncertainties in simulated dust emission, transport and removal processes are also possible factors for the disparity between model results and local experimental data [*Fairlie et al.*, 2007]. Figure 2b shows that the model simulates realistically the total iron evolution, suggesting validity of our initial estimate of fixed total iron content in the soil at the source region. Differences between model results and in situ data for dust laden total Fe seen on Figure 2b are likely attributable to the above mentioned underestimation of dust concentration. Also, note that the total iron measured at Kosan site under non-dusty conditions could be enhanced by anthropogenic sources [*Chuang et al.*, 2005] as discussed below.

[33] Figure 2c compares model predictions for total Fe concentrations with those measured on the Ron Brown farther east from continental Asia (note approximately 1 day delay in peak dust concentration). Figure 2d shows that that total iron concentrations even farther east in the Pacific are still reasonably simulated when compared to C05 measurements. One exception is 19 April when model significantly underestimated total iron. The large measured values are most likely related to the previously mentioned 10 April event. During the transport of this intense dust event, the

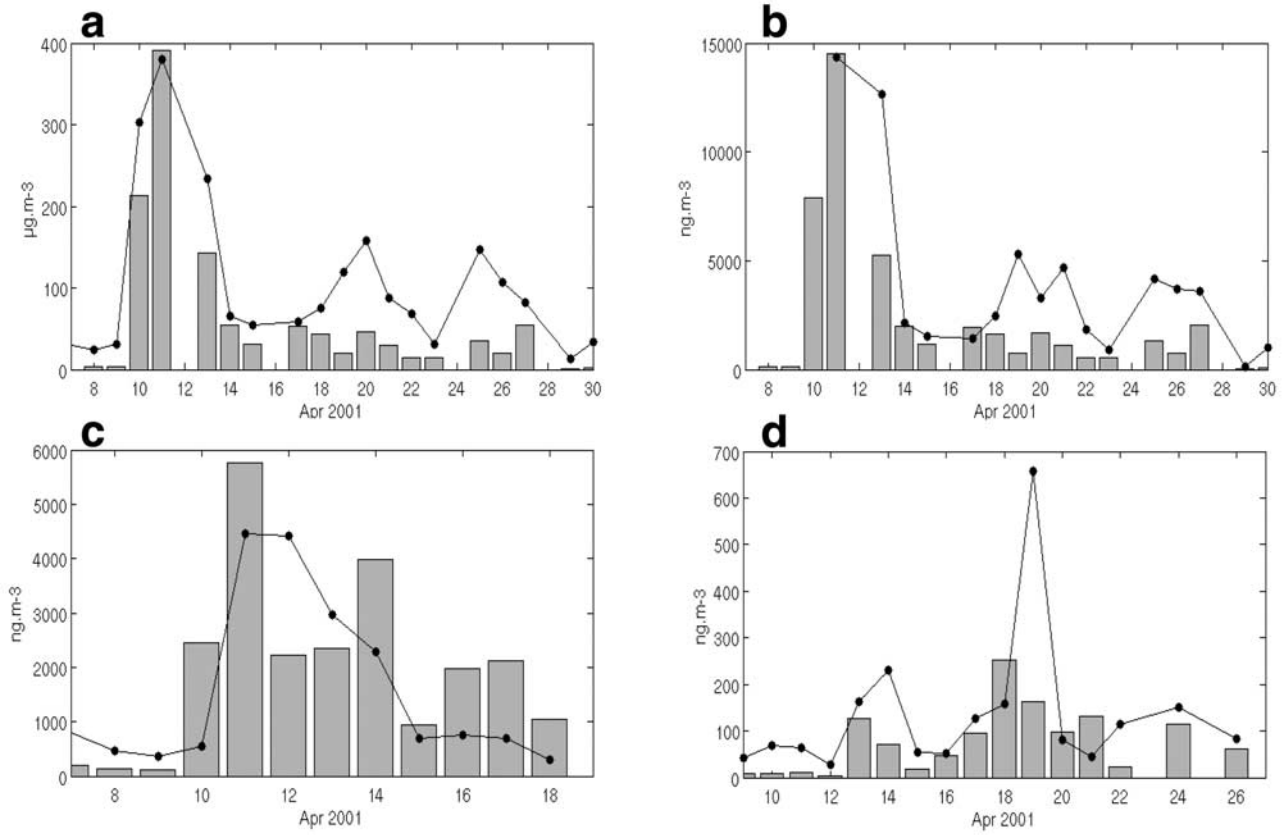

Figure 2. Simulated (bar) versus measured (dot line) dust and total iron concentrations during April 2001. (a) Mineral dust (crustal material) over Kosan. (b) Total iron over Kosan. (c) Total iron during the RB cruise. (d) Total iron during the C05 cruise.

model shows a strong concentration gradient in the mid-Pacific (data not shown). The underestimation of the concentration peak, which is measured locally, could be due to inaccuracy in simulated transport/diffusion of the plume. Overall, the model and measurement comparisons of total aerosol mass and iron content at Kosan, onboard the R/V Ron Brown and in the remote Pacific for are considered sufficiently realistic for the purposes of this study.

3.1.2. Sulfate

[34] Dissolved sulfates play a major role in the acidification of the dust aqueous phase and subsequent dissolution of dust minerals. In this section, we perform an evaluation of model results against aerosol sulfate observations available in the above mentioned data sets.

[35] Aerosol analysis performed at the Kosan supersite during ACE-Asia are related to the total suspended matter and compared directly with model results (recall the latter accounts only for PM12). Figure 3a displays the measured total nss-sulfate concentrations against simulated particulate sulfate species, namely anthropogenic sulfate, dust mode sulfate and sulfate bound to $CaSO_4$ (the latter is not dissolved) over Kosan. Overall, the total soluble sulfate (anthropogenic + dust-SO_4), is underestimated which can possibly point out to basic model uncertainties like emission underestimation or some transport/removal issues affecting aerosol plumes when comparing to local measurements (in section 3.2.4 and Table 3, we show through a sensitivity study that an increase of SO_2 emission can indeed result in an enhancement of dust mode dissolved sulfate). However, if we include sulfate bound to dust-$CaSO_4$ in the model/measurement comparison (Figure 3a), we see that this sequestrated sulfate could also account for a significant fraction of the model discrepancy, especially during dust dominated events. In our simulation, dissolved dust-SO_4 concentrations are almost zero during the intense dust event due to the strong calcium buffering (10–13 April, Figure 3a), whereas soluble sulfate is still observed in association with dust in the Kosan measurements [see also *Arimoto et al.*, 2006; *Sullivan et al.*, 2007]. It may be possible that a fraction of $CaSO_4$ could exist in a soluble form, or be dissolved during laboratory extraction of water-soluble ions. However, if we do not consider this hypothesis, the comparison with measurements suggests that SO_2 scavenging could be underestimated in the model, or that a fraction of formed gypsum should remain soluble. This comparison is incomplete due to the fact that there is no experimental data of gypsum content from Kosan. We note that the simulated soluble dust-SO_4 fraction tends to increase for lower intensity dust events (14–24 April, Figure 3a), outlining that the dust buffering capacity has been reached in the model and that simulated dust-SO_4 starts to accumulate significantly in solution.

[36] Comparisons of model results with Ron Brown super-micron measurements (Figure 3b) for nss-sulfate are qualitatively similar to those from Kosan. Since these measurements isolate the super-micron particles, we assume

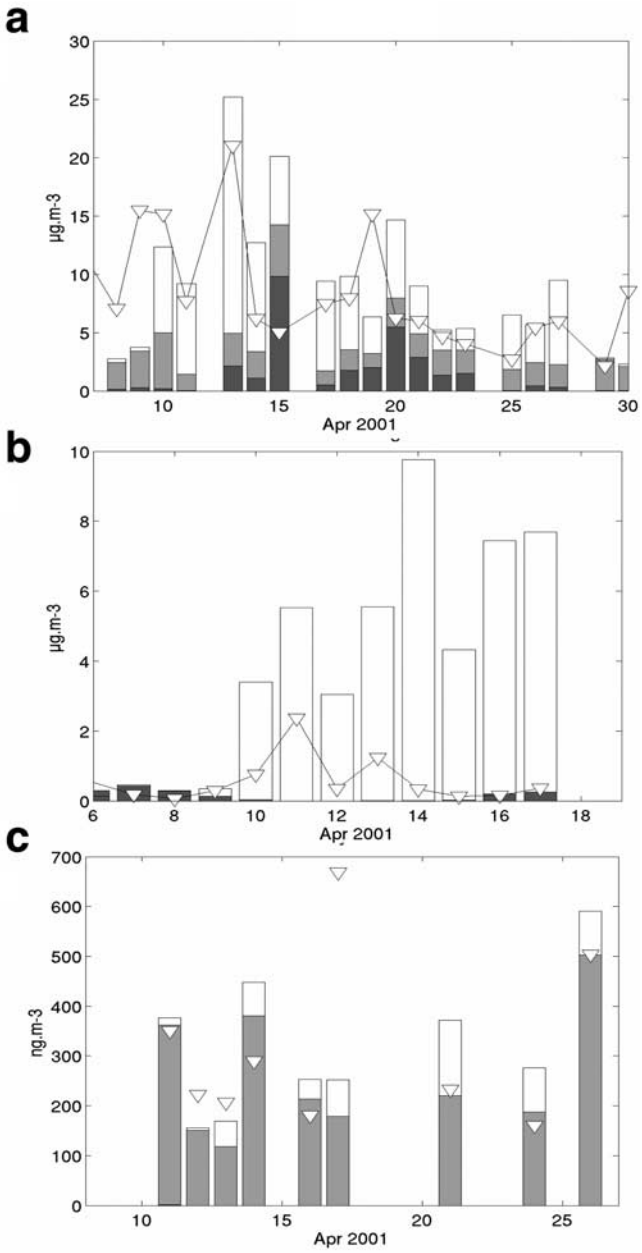

Figure 3. Simulated versus measured concentrations for major soluble ions at (a) Kosan supersite, (b) Rob Brown cruise, (c) C05 cruise. For non-sea-salt sulfate simulation, several contributions are plotted: Dust-SO_4 is represented by the black bar; anthropogenic SO_4 fraction, by the gray bar; and Dust-$CaSO_4$, by the white bar. Measurements are represented by the triangle symbols. For Kosan, measurements represent total suspended matter. For Ron Brown, measurements represent super micron particles (most likely associated with dust). For C05, measurements represent PM10 particles.

that all measured sulfate is here associated with dust particles and thus directly comparable to simulated dust-SO_4. During the main dust event the RB measurements show some peak in nss-sulfate associated with dust, whereas simulated dust-sulfate are mostly bound to dust-$CaSO_4$. Again, the possibility that a fraction of simulated gypsum actually remains in solution or is being extracted to solution during aerosol analysis could explain the discrepancy between model and measurements for the large dust event (10–14 April, Figure 3b).

[37] Figure 3c presents a comparison of simulated sulfate to C05 nss-sulfate measurements in the mid-Pacific. Measurements show large nss-sulfate concentrations that could result from transport of pollution from East Asia or Hawaii, as well as local formation from DMS oxidation [*Prospero et al.*, 2003]. The soluble sulfate simulated by the model resides mostly in the anthropogenic mode and is reasonably consistent with measurements. As outlined in C05, soluble nss-sulfate is not as strongly correlated to dust than it is for Kosan and RB data sets during intense dust outbreak due to different sulfate source contributions. Hence it is actually difficult to assess from the observations which fraction of sulfate is associated with dust and to evaluate whether the model underestimates the dust-sulfate fraction.

3.1.3. Other Ions

[38] Numerous studies have outlined the efficiency of HNO_3 scavenging by dust [e.g., *Jordan et al.*, 2003]. In Figure 4a, it is observed that most of the simulated dissolved nitrate is associated with dust (high fraction of dust-NO_3 compared to anthropogenic NO_3) especially during the most intense dust event (10–13 April). As outlined previously for the Kosan data set, dust concentrations tend to be underestimated. As most of the nitrate is associated with dust, the dust concentration underestimation could lead directly to an underestimation of dust-NO_3 compared to measurements, especially for 13 April and 19–26 April period (see Figures 2a and 4b). Inversely when comparing to the RB data (Figure 4b), dust-NO_3 are overestimated mainly for 10–11 April when total iron concentrations (and likewise dust concentrations) are overestimated. If we normalize dust-NO_3 by dust concentrations, the agreement between model and measurement becomes better for both data sets (data not shown). During the prefrontal period (8–9 April), *Arimoto et al.* [2006] showed that measured NO_3 during the RB cruise is mostly associated with sea salt, whose contribution is not accounted for in this model comparison. After 9 April, however, the sea salt nitrate contribution is much less significant and therefore is unlikely to strongly affect these comparisons.

[39] For both Kosan and RB comparisons, simulated dust-NO_3 show similar patterns to dust-Ca^{2+} (Figures 4a, 4b and 5a, 5b), which is consistent with observations and thermodynamic equilibrium [see also *Arimoto et al.*, 2006;

Table 3. Measured and Simulated Average Concentrations of Particulate Sulfate for the Kosan, Ron Brown and Chen (2005) Locations[a]

		MES ($\mu g\ m^{-3}$)	Dust-SO_4 ($\mu g\ m^{-3}$)	Dust-SO_4 + anthropogenic SO_4 ($\mu g\ m^{-3}$)
Kosan	REF	8.1	1.6	3.9
	$SO_2 \times 2$		3.4	7.6
RB	REF	0.4	0.2	
	$SO_2 \times 2$		1.2	
C05	REF	0.3	0.2E-3	0.25
	$SO_2 \times 2$		0.5E-3	0.35

[a]Simulated sulfate is reported for anthropogenic and dust mode (except for RB data which is in dust mode only, see text) and for present-day condition simulation and 2 × SO_2 simulation.

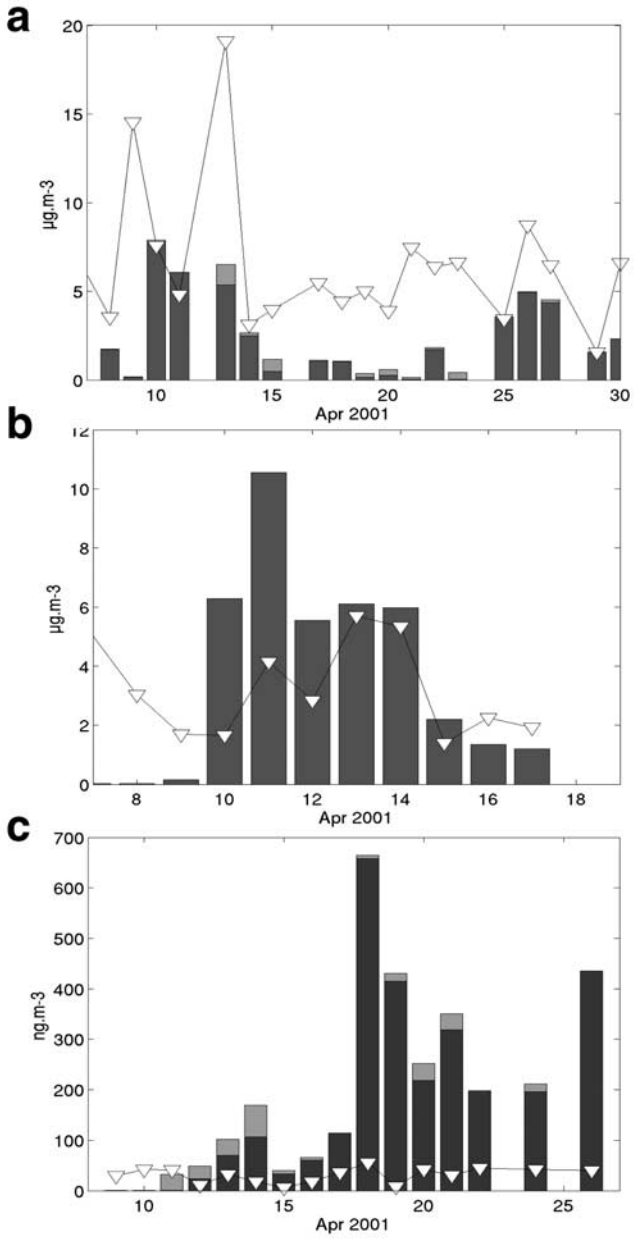

Figure 4. Simulated versus measured concentrations for particulate nitrate (a) Kosan supersite, (b) Rob Brown cruise, (c) C05 cruise. Simulated Dust-NO_3 is represented by the black bar; anthropogenic NO_3, by the gray bar. Measurements are represented by the triangle symbols. For Kosan, measurements represent total suspended matter. For Ron Brown, measurements represent super micron particles (most likely associated with dust). For C05, measurements represent PM10 particles.

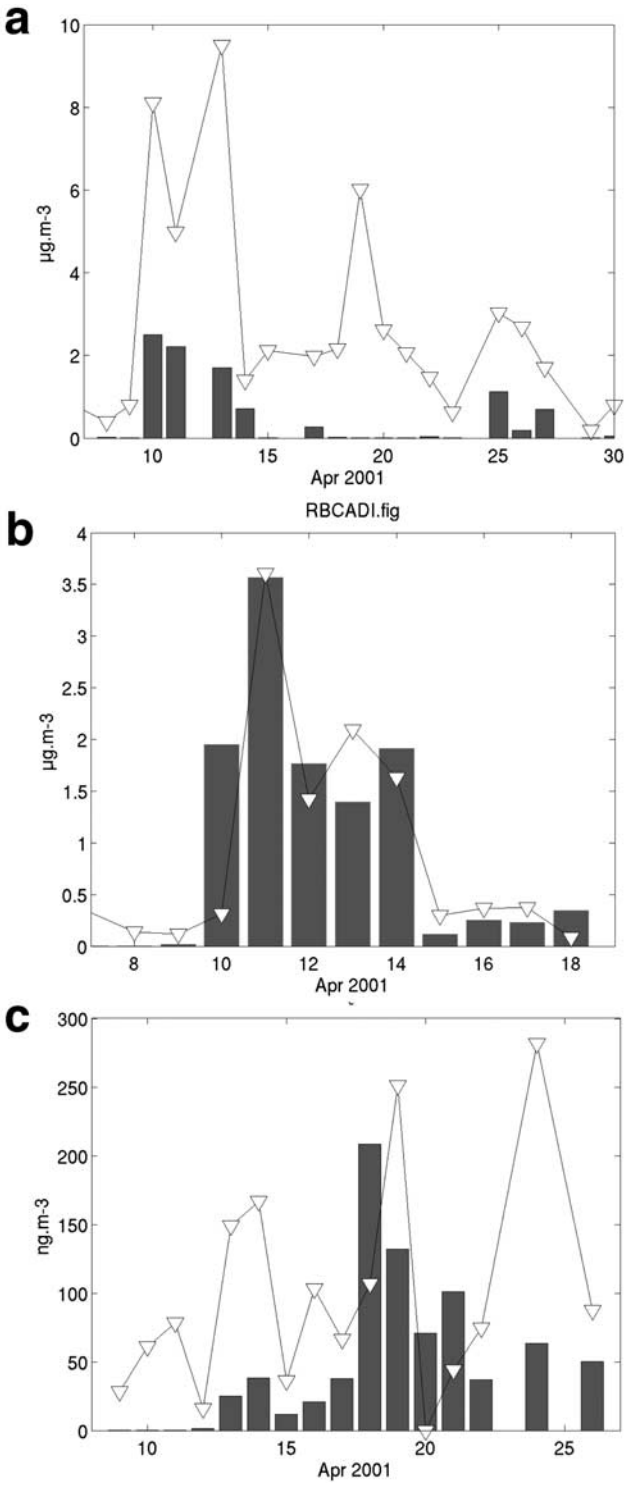

Figure 5. Simulated versus measured concentrations for calcium cation at (a) Kosan supersite, (b) Rob Brown cruise, (c) C05 cruise. Simulated Dust-Ca^{2+} is represented by the black bar. Measurements are represented by the triangle symbols. For Kosan, measurements represent total suspended matter. For Ron Brown, measurements represent super micron particles (most likely associated with dust). For C05, measurements represent PM10 particles.

Kline et al., 2004]. Dust-Ca^{2+} results from the equilibrium between acidic uptake, $CaSO_4$ precipitation and pH-dependant calcite dissolution. For the Kosan data, gypsum formation results in a lower dust-Ca^{2+} which, by thermodynamic equilibrium, leads to a reduced HNO_3 uptake compared to observations (Figure 4d). The simulation of both dust-NO_3 and dust-Ca^{2+} tends to be better when compared to RB data during the 10–18 April dusty period. As a cruise samples

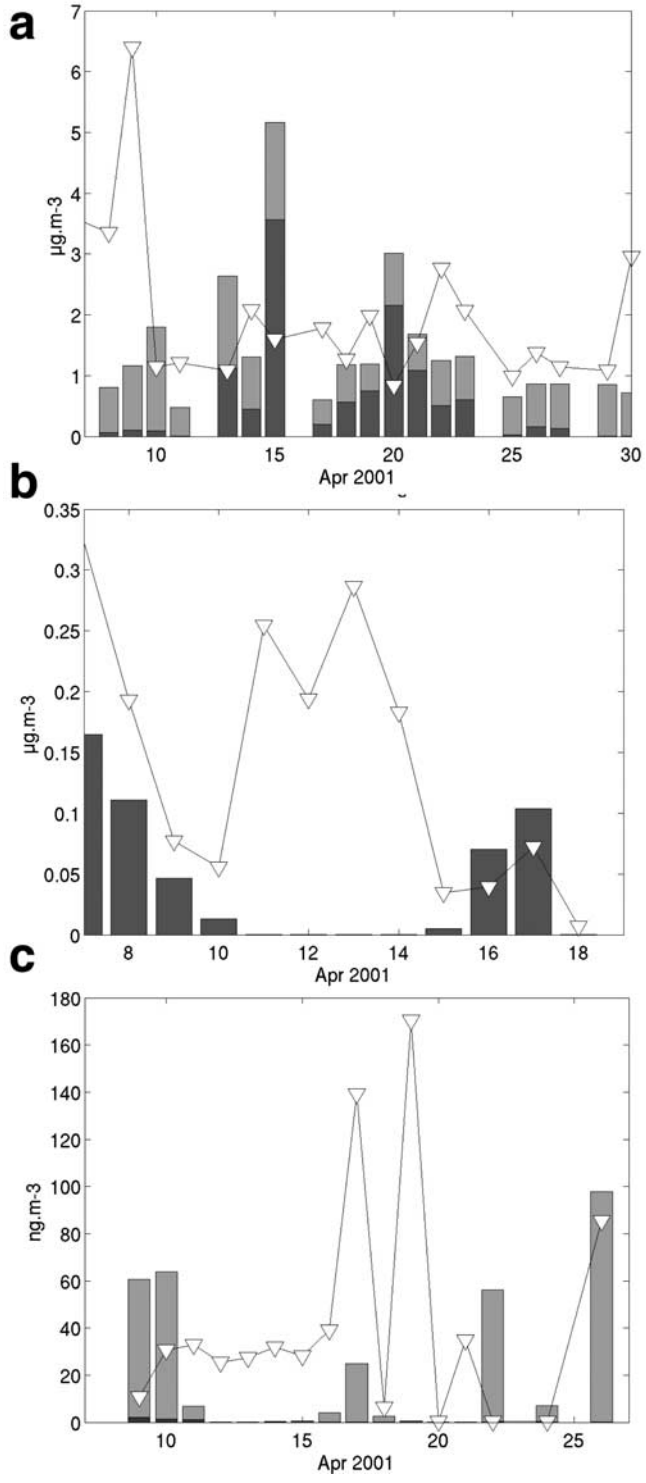

Figure 6. Simulated versus measured concentrations for ammonium particulate at (a) Kosan supersite, (b) Rob Brown cruise, (c) C05 cruise. Simulated Dust-NH_4 is represented by the black bar; anthropogenic NH_4, by the gray bar. Measurements are represented by the triangle symbols. For Kosan, measurements represent total suspended matter. For Ron Brown, measurements represent super micron particles (most likely associated with dust). For C05, measurements represent PM10 particles.

different geographical locations, any local transport biases might be smoothed out in this case.

[40] Compared with C05 data over the remote Pacific, Figure 4c shows a large overestimation of soluble NO_3 simulated by the model, which is primarily formed in the dust mode. However, C05 outline that measured nitrate concentrations are rather low and tend to be in conflict with long-term observations of Midway Island [*Prospero et al.*, 2003] reporting an average concentration of 480 ng m^{-3} for April (1981–2001), which is much more consistent with our model results. Figure 5c shows that dust-Ca^{2+} are quite consistent with measurements. This suggests that, unlike for Kosan and RB observations, C05 data do not show a strong evidence of soluble nitrate being associated to dust whereas the model does. The reason for this discrepancy is not totally clear to us.

[41] The behavior of simulated dust-NH_4 matches dust-SO_4 since uptake of NH_3 is most efficient when the dust has been previously acidified [*Sullivan et al.*, 2007; *Song and Carmichael*, 2001]. Because of this, when dust-Ca^{2+} content is large compared to dust-SO_4, dust-NH_4 tends to volatilize out of solution and eventually condense again in the anthropogenic mode. At Kosan, simulated NH_4^+ resides primarily in the anthropogenic mode (Figure 6a), and the amount ammonium is relatively well-simulated after the frontal passage. The super-micron Ron Brown data (Figure 6b) indicates that the ammonium concentration should be higher in the dust mode than is simulated by the model. The precipitation and neutralization of simulated dust-SO_4 during the large dust event did not allow for a pre-acidification of dust and therefore efficient NH_3 uptake, in apparent contrast with the data. This argument holds when comparing the model results to C05 data (Figures 6c and 3c), where both simulated soluble dust-NH_4 and dust-SO_4 concentrations are also low compared to observations.

[42] Overall, the simulated behaviors of major soluble ions show some consistency with surface concentrations measurements. The major problem arising is that neutralization of simulated dust-SO_4 appears to be overly efficient during big dust events in the continental outflow, when observations still show soluble sulfate associated with large dust concentrations [see also *Arimoto et al.*, 2006]. It is possible that a fraction of gypsum can stay in solution when the model causes it to precipitate, or that the SO_2 scavenging rate and therefore soluble sulfate is underestimated. Unfortunately, available data cannot constrain these hypotheses since the solid $CaSO_4$ fraction was not explicitly measured. The precipitation of gypsum in a given particle and at a given time depends on concentrations dust-Ca^{2+} and dust-SO_4 ratio and hence from the chemical history of the particle including different gases scavenging, mineral dissolution and equilibrium processes. As outlined in the data analysis by *Sullivan et al.* [2007], this history can be very complex and still very challenging for modeling, even using the most comprehensive schemes. The representation of chemical processes is also complicated by the fact that a CTM model grid box is supposed to be well mixed which is not necessarily the case for an observation station situated relatively close to intense sources.

[43] In the next sections, we use the model to explore further dust-pollution interactions and their effect on iron

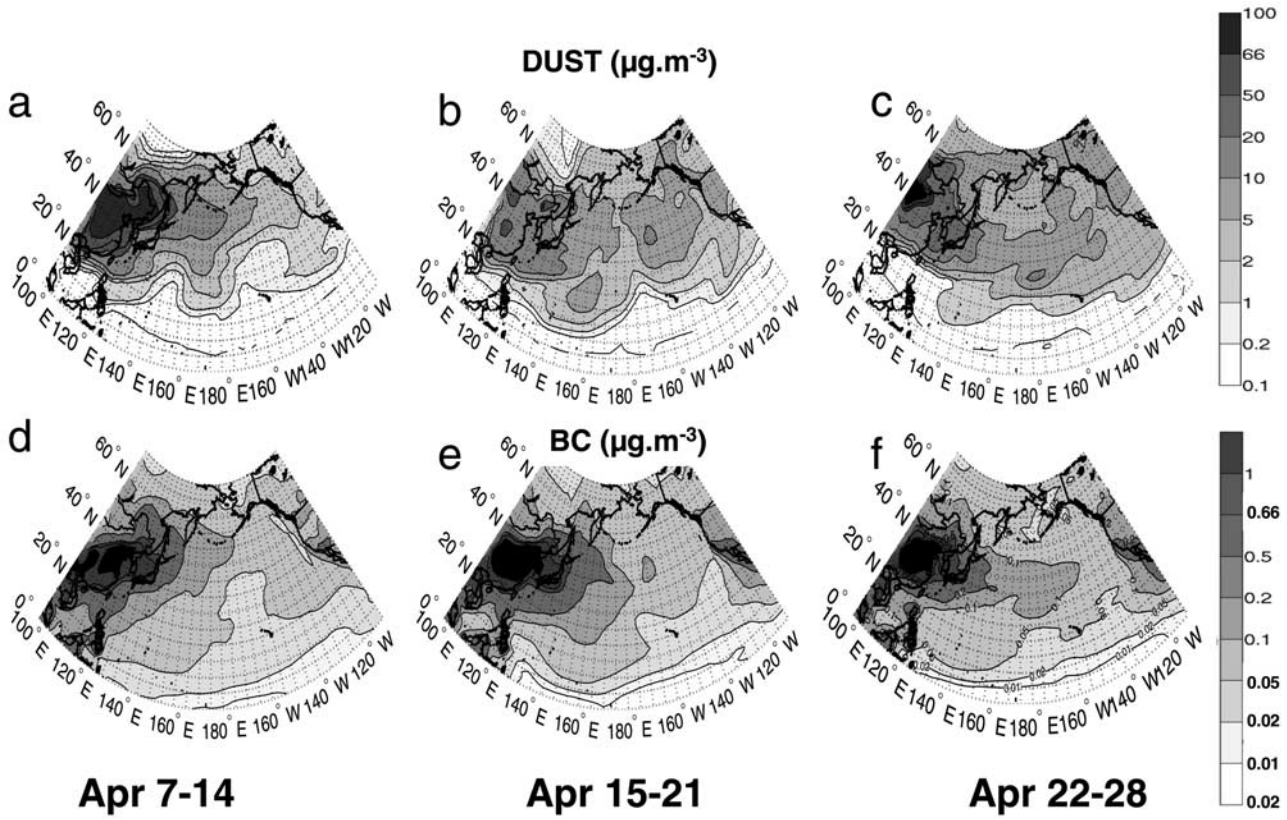

Figure 7. Vertically and weekly averaged tropospheric concentrations obtained with GEOS-Chem simulations for the three reference weeks during April 2001 (see text). (a, b, c) Dust mode concentrations. (d, e, f) Anthropogenic black carbon concentrations.

dissolution at the scale of NPO basin. The impact of the potential model biases identified in this section on these results will be discussed as part of this analysis.

3.2. Simulation of Mineral Dissolution and Dissolved Iron Concentrations Over the NPO

[44] Following *Heald et al.* [2006a] we have identified three characteristic periods during April 2001 (Figure 7).

[45] 1. During 7–14 April, intense dust transport over the North Pacific and predominantly the western (west of 180 E) part of the domain (Figure 7a) dominates.

[46] 2. During 15–21 April, the dust concentration over the western part of the domain drops, whereas pollution levels tend to increase (Figures 7b, 7e). The eastern part (east of 180 E) of the domain shows significant amount of dust transported from the previous week and limited pollution.

[47] 3. During 22–28 April, a weaker dust event begins over continental east Asia, whereas dust concentrations over the central and eastern Pacific remain moderate. However, larger simulated black carbon (BC) concentrations over the middle and eastern Pacific indicate strengthened trans-Pacific pollution transport (Figures 7c, 7f). For each of these three characteristic weeks, we discuss the evolution of simulated mineral dissolution over the domain.

3.2.1. Dust Acidity Buffering and pH Evolution

3.2.1.1. During 7–14 April

[48] This period is characterized by large dust concentrations over east Asia, specifically the region 35–55 N, 100–140 E. The fraction of calcite to total calcium in the dust mode remains large for this region (Figure 8d), whereas the $CaSO_4$ fraction is fairly small (Figure 8g). This indicates that the $CaCO_3$ alkalinity reservoir remains large in this region and is able to buffer all the acidity linked to anthropogenic emissions. Consequently, average pH values remain high over this source region (Figure 9a).

[49] Southward, in the region 15–35 N and 100–140 E, the decrease of dust concentrations and the increase of pollutant concentrations over southern China result in a decrease of $CaCO_3$ fraction. This gradient is associated with a conversion of the alcite pool to enhance dust-Ca^{2+} and dust-$CaSO_4$ fractions (Figures 8a, 8d and 8g), allowing also more anions to be in solution and leading to decreased pH values.

[50] Moving eastward to the NPO (140 E to 140 W), the calcite fraction tends to slowly decrease (Figure 8d) indicating the progressive aging of dust. This aging tends to be enhanced on the southern edges of the dust outflow where the pollution levels are larger with a resulting acidification of dust particles (Figure 9a).

3.2.1.2. During 15–21 April

[51] Compared to the previous week, the average dust concentrations are much lower (but still significant) over continental east Asia and western Pacific regions, where large amounts of pollutant are also present (Figures 7b, 7e). The relative amount of dust-$CaSO_4$ formed is maximum in the window 20–40 N; 100–140 E, indicating a large reduction of the calcite pool (Figures 8e, 8h). Because the

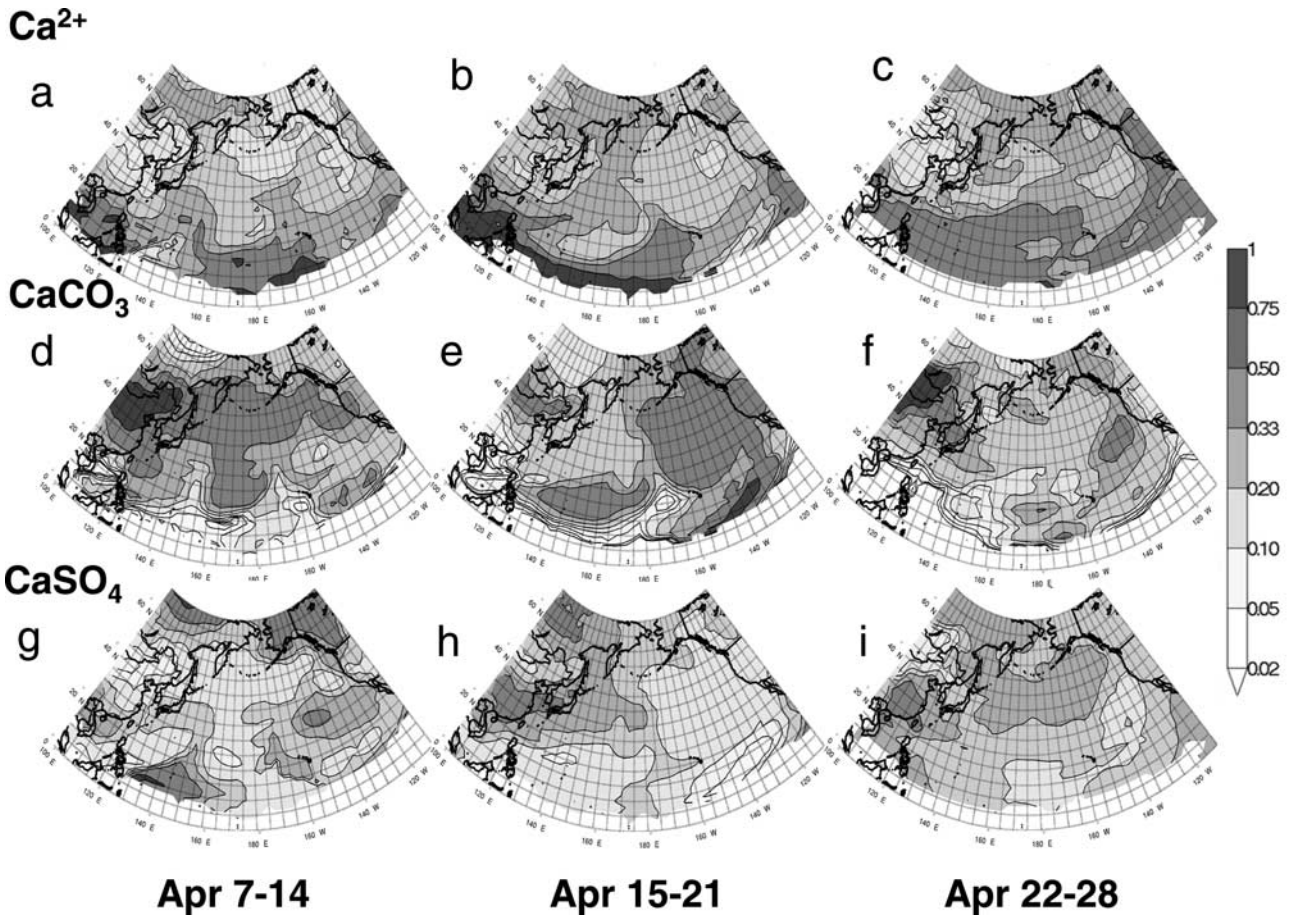

Figure 8. Vertically and weekly averaged partition of calcium (molar ratio) into calcium cation (dust-Ca^{2+}), calcite (dust-$CaCO_3$) and gypsum (dust-$CaSO_4$) for the three different regime of April 2001.

buffering capacity of dust is exceeded, an enhanced acidification of the particles can be observed with a decrease in simulated pH (Figure 9b) over southern China.

[52] On the eastern part of the Pacific basin (east of 180 W), the simulation shows higher values of calcite present in dust which results from the previous week's large dust event advected over the basin. The amount of $CaSO_4$ formed has also reached a limit in this area, indicating that dust issued from the large event occurring on 15–21 April did not undergo any significant additional mineral dissolution while advecting over the Pacific. This is illustrated directly by the average pH fields (Figure 9b) which remains large and almost unchanged compared to the source dust pH. A fraction of the large dust plume has been also transported farther to the south, where it forms a local calcite and pH maxima in the 10–25 N and 140–180 E region.

3.2.1.3. During 22–28 April

[53] The east Asia source region (100–120 E) is characterized by the beginning of a new dust event, and the prevailing dust regime is similar to the 7–14 April regime over the dust source continental area. Over the NPO basin, the dust exhibits relatively low calcite fractions (Figures 8c, 8f and 8i) associated with an enhanced $CaSO_4$ fraction. This indicates that dusty air masses from the 22–28 April have a weaker buffering capacity and therefore a higher potential for acidification. This acidification is enhanced over the 5–20 N; 100E–160W region of the domain as shown on the average pH field (Figure 9c).

3.2.2. Soluble Iron and DIF Evolution

[54] The dissolved iron concentration plotted in Figures 9d, 9e and 9f depends on the dust amount, which determines the total iron concentration, and the dissolved iron fraction (DIF, section 2). Part of the DIF (0.45%) is fixed as the initial condition and the other part results from chemical processing. For 7–14 April, relatively large concentrations of dissolved iron are found over the source region where dust concentrations are the largest (Figures 9d and 7a). For this region and north of 30 N (Figure 9g), the DIF is very close to its initial value of 0.45% indicating that no significant processing occurred due to the acidity buffering effect discussed previously. South of 30 N on Figure 9g, a slight enhancement of DIF resulting from the interaction with anthropogenic acidic compounds is visible. Accordingly, the relative contribution of soluble iron due to atmospheric processing is larger for this region.

[55] DIF enhancement becomes more intense for 15–21 and 21–28 April cases while transitioning from an intense dust regime to a lower dust regime (Figures 9h, 9i). During 22–28 April, the average dissolved iron fraction ranges from 1 to more than 6 % over the NPO, with the highest values close to major anthropogenic sources. The local maximum of dissolved iron visible in the mid-Pacific on Figure 9f results from a significant amount of dust that has

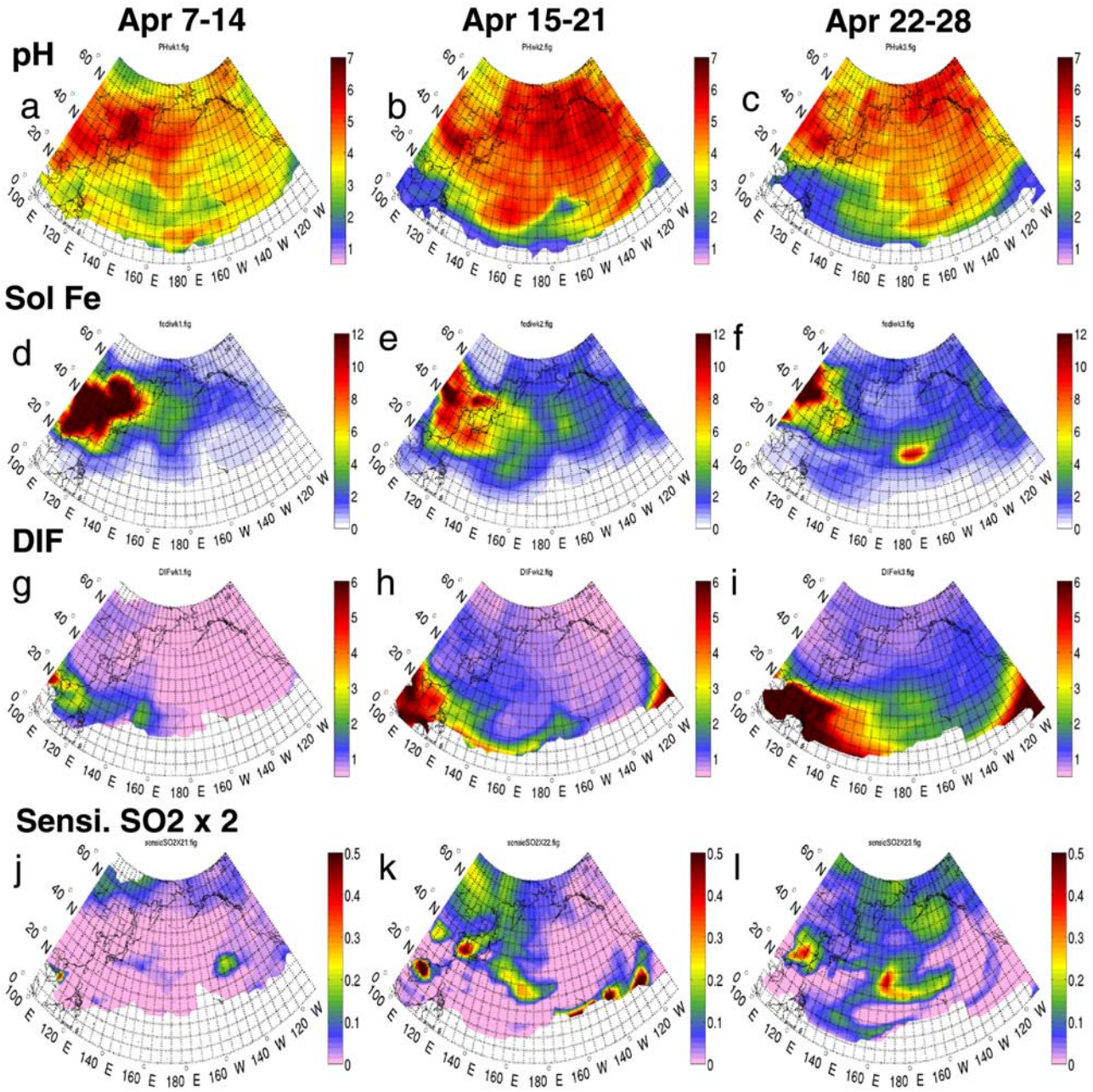

Figure 9. Vertically and weekly averaged dust-pH, dust-soluble iron concentration and dust-dissolved iron fraction for the three different regime of April 2001. (a, b, c) Simulated dust mode pH, contours are plotted for dust concentration above 100 ng m^{-3}. (d, e, f) Simulated soluble iron concentrations (in ng m^{-3}). (g, h, i) Simulated dissolved iron fraction (in percentages). Contours are plotted for dust-soluble iron concentrations exceeding 0.2 ng m^{-3}. (j, k, l) Sensitivity of soluble iron production to a doubling of SO_2 sources. Fraction defined as (DIF ($SO_2 \times 2$) − DIF)/DIF.

interacted with pollution and has gone under significant iron processing to reach an averaged DIF of almost 3%. If we consider the initial DIF contribution (0.45%), it means that ~84% of soluble iron present in this air mass was produced via dust pollution processing under our model assumptions.

[56] According to these model results, we see that the moderate dust regime is more efficient for producing soluble iron (via interaction with anthropogenic pollution) during transport over the remote Pacific than the intense dust regime. This result is in line with M05 box model study except that it is illustrated here in a spatially resolved way.

3.2.3. Comparison With Soluble Iron Measurements During April 2001

[57] How realistic are the soluble iron concentrations produced by the model? To address this question, we use data from the Kosan [*Chuang et al.*, 2005] and C05 data sets which provide measurements of soluble iron during the April 2001 period.

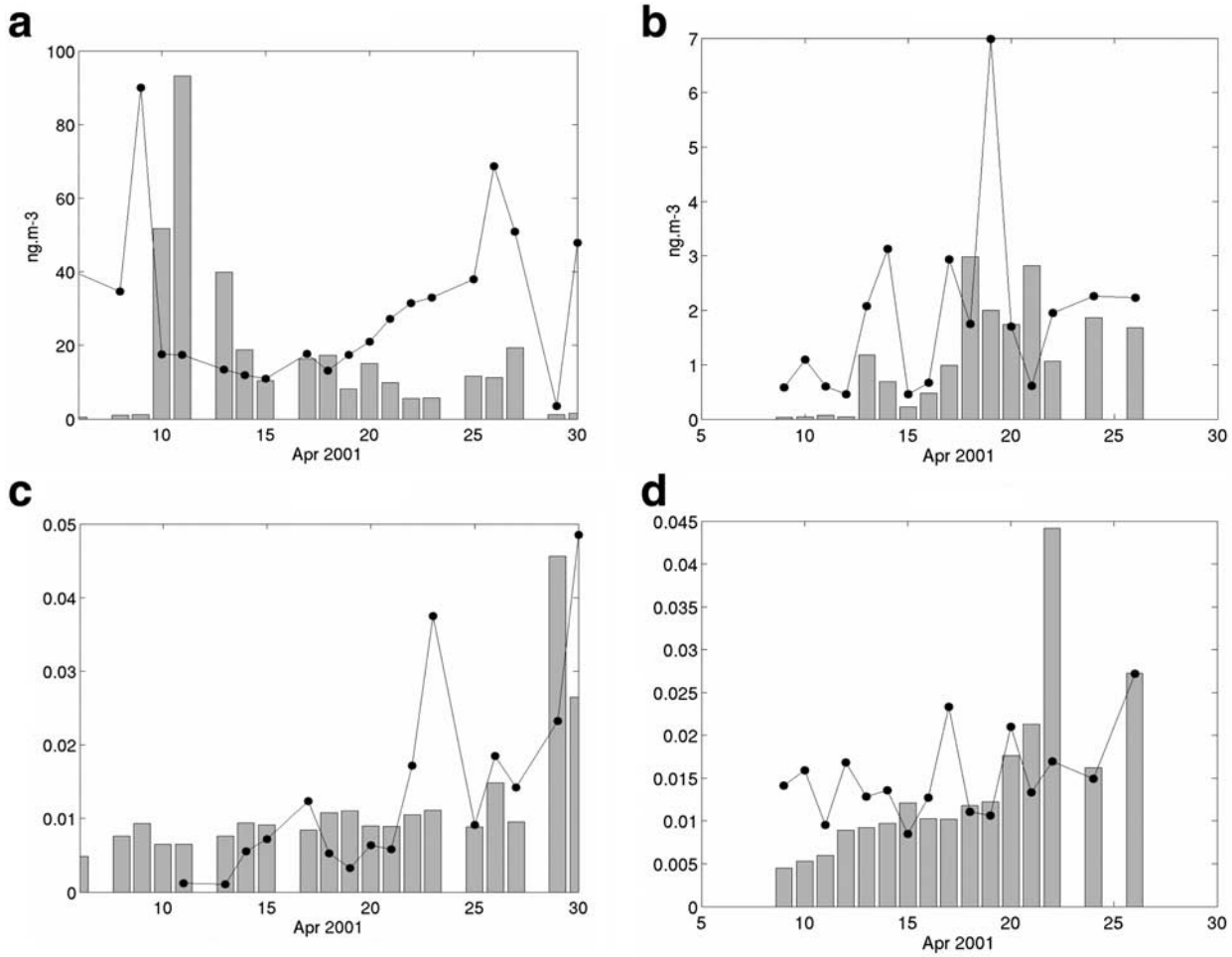

Figure 10. Simulated (bar) versus measured (dot line) soluble iron concentrations in surface and corresponding dissolved iron fraction (unitless) during April 2001. (a) Soluble iron concentration over Kosan. (b) Soluble iron measured during the C05 cruise. (c) Dissolved Iron Fraction (DIF) over Kosan. (d) Dissolved Iron Fraction (DIF) during the C05 cruise.

[58] Model results are compared to these measurements in Figure 10. Despite comparable magnitudes, soluble iron measurements and simulations over Kosan show noticeable discrepancies (Figure 10a). Simulated soluble iron follows the simulated dust concentrations, largest values being obtained during the intense dust event of 10–14 April on Figure 10a. However, Kosan soluble iron measurements don't show any obvious correlation with total iron. When analyzing this data set, *Chuang et al.* [2005] showed that soluble iron was primarily correlated to black carbon, from which they deduce that there exists a dominant (relative to mineral dust) combustion-derived soluble iron source. On the basis of these results, the potential magnitude of dissolved iron associated to BC has been studied by *Luo et al.* [2008] who conclude that this source could indeed be significant compared to dust close to the largest pollution sources of east Asia. In the present simulation, the soluble iron associated with BC is not accounted for and that could be one reason for the discrepancy between model and measurements. A second reason will also be discussed below.

[59] Besides soluble iron concentrations, it is also important to focus on the DIF which characterize the chemical processing efficiency for dissolved iron production. Figure 10c suggests that the model overestimates the dissolved iron fraction during the intense dust event (10–13 April). Because almost no processing occurs in the simulation due to strong buffering effects over Kosan area during the intense dust front, this could point out a problem in setting an initial value for the dissolved iron fraction. The initial DIF is based on measurements from one sampling site. As stated in section 2, these measurements exhibit a range of 0.05 to 1% at the Dunhuang site, which demonstrates that variability in initial DIF can explain the discrepancy in simulated and observed DIF during the large dust events. Given that dust measured in Kosan can be emitted from different regions, it seems likely that an even larger variability in the actual initial DIF can be found. Again, not including combustion iron in the model is another possible source of DIF biases.

[60] Because simulated and observed DIF are relatively comparable for the period of 19 to 30 April, the underestimation of total iron concentration (compare discussion in section 3.1.1 and Figure 2b) partly explains the underestimation of dissolved iron concentration. This underestimation may also be partly due the absence of the anthropogenic iron source in the model.

[61] The better agreement of simulated versus measured DIF, which both show an increasing trend during the moderate dust regime, could be explained by a point raised in the study by *Chuang et al.* [2005]: under certain conditions, iron processing can be responsible for a strong observed correlation between dust-soluble iron and pollutants (for which BC is a good tracer), while dust and total iron are poorly correlated. Such a correlation could be obtained if pollutants that convert insoluble iron to soluble forms are limiting. In the case of Kosan data, isolating the fraction of dissolved iron directly emitted with anthropogenic BC from the fraction of dust dissolved iron formed in acidic air masses rich in BC is not really possible and would require more observations as well as finer modeling studies. In either case, however, anthropogenic pollution plays a central role in forming soluble iron.

[62] In the remote Pacific region, Figures 10c and 10d show model output versus C05 measured concentrations of soluble iron and associated DIF. C05 measured concentrations are quite large compared to typical conditions as a result of the intense trans-Pacific dust transport from east Asia. C05 analysis showed also that soluble iron concentrations were strongly correlated to dust during the cruise, which facilitates here the comparison and interpretation of model results, as it appears that anthropogenic soluble iron is less important. Simulations of soluble iron are reasonably consistent with observations as seen in Figure 10b, both in magnitude and trend. The underestimation of simulated soluble iron appearing on 19 and 9–12 April is mainly due to the previously discussed total iron underestimation (Figure 2d). The simulated DIF (Figure 10d) is also underestimated before 12 April, but the impact of this underestimation is balanced by the fact that both model and concentration in dust and total iron are very low for these days. Simulated and measured DIF evolution are relatively consistent from 15 to 26 April. Simulated DIF shows a slightly increasing trend from 19 to 26 April as the dust to pollution ratio tends to decrease (compare Figure 10d and section 3.2.1). A slightly increasing trend can be also seen in the C05 DIF measurements on the same period, although it is obviously difficult to conclude with such a short time series. This does support the importance of acidic processing for soluble iron deposition to the remote NPO.

3.2.4. Sensitivity of Dissolved Iron Fraction to Anthropogenic SO_2 Sources

[63] Understanding how soluble Fe content of mineral dust may be influenced by variations in anthropogenic emissions is important considering the rapidly increasing emissions in East Asia [*Ohara et al.*, 2007]. We performed a test in which we ran a simulation with doubled SO_2 emissions for April 2001, all other conditions remaining unchanged, and compared it to the test case studied in previous sections. Such a doubling of SO_2 emission is considered to be reached, or even exceeded, by 2020 in SRES A1B and A2 emission scenarios [*Nakicenovic et al.*, 2000].

[64] We find that, on average, an SO_2 emission increase results in a significant increase of dust mode dissolved sulfate over the different measurements sites (Table 3). This demonstrates that, as expected, enhanced SO_2 emissions results in enhanced sulfate scavenging, and that uncertainties on simulated dust mode sulfate content are strongly dependant on uncertainties on sulfur emissions. We examine hereafter the consequences of enhanced SO_2 scavenging by dust on soluble iron production.

[65] Figures 9j, 9k and 9l display the mean relative difference of dissolved iron production between the $SO_2 \times 2$ simulation and the reference case for the three weeks of April 2001. This fraction can be interpreted as a relative change of dissolved iron concentration or, equivalently, dissolved iron fraction, since total iron remains unchanged between the two cases.

[66] During the intense dust event (7–14 April, Figure 9j) the relative increase of dissolved iron production remains globally limited and virtually unchanged in the high dust region. In spite of a doubling of SO_2 emissions, the buffering effect of dust in this situation is still sufficient to prevent dust acidification and iron dissolution over most of the dust region. A limited enhancement ($\sim$5%) of dissolved iron production can nevertheless be observed locally in the outflow in the 35 N 140–160 E region.

[67] During 15–21 April, this high dust/low pollution air mass is now located on the eastern part of the basin (east of 180W), and therefore this region does not exhibit a significant sensitivity to SO_2 doubling on Figure 9k. However, in the region to the west of 180 W, we obtain a significant enhancement of dissolved iron production, ranging between 10 and 40%. Over the ocean, the enhancement tends to be larger along 25 and 35 N pointing out a sensitive area in term of dust-pollution interactions. It is worth noting that some regions showing already a high DIF in the reference case, like the southeastern part of the domain on Figures 9h and 9k, do not show a strong sensitivity to SO_2 emission doubling. For these regions, it is likely that dust solution was already acidic in present-day conditions. Consequently the rate of hematite dissolution was already close to its maximum value and did not undergo any significant increase.

[68] Finally, the week of 21–28 April shows the most significant increase in soluble iron production. The characteristic middle Pacific maximum region pointed out previously (Figure 9f) exhibits an enhancement in dissolved iron production of 20 to 40 % (Figure 9l). Interestingly, we see a significant increase of soluble iron production of about 25% in the vicinity of the Aleutian islands, a sub region studied hereafter.

[69] For April 2001, the evolution of regional dissolved iron deposition under SO_2 doubling conditions matches the evolution of DIF. In order to quantify this evolution, we present in Table 4 the dissolved iron deposition flux (wet and dry deposition as detailed in section 4) averaged over April 2001 and for two regions of the domain materialized on Figure 1: (1) the NPO region (3–65N; 120 E–115W) and (2) a remote Pacific region (40–60N; 135–170W) roughly representing a well-identified HNLC region [*Moore et al.*, 2002; *Meskhidze et al.*, 2005]. According to the model, a doubling of SO_2 emissions would induce a monthly averaged increase in soluble iron deposition of 6% for the NPO domain, and 13 % for the remote HNLC domain. These results suggest a potentially important role of future changes in anthropogenic activity in the iron budget of remote marine ecosystems. However, this role will also

Table 4. Soluble Iron Deposition Averaged Over North Pacific Ocean Domain and HNLC Region (see Text and Figure 1) for April 2001 and Under Present-day and 2 × SO_2 Emission Scenarios

	Soluble Fe Deposition (mg m^{-2} a^{-1}) REF	Soluble Fe Deposition (mg m^{-2} a^{-1}) SO_2 × 2	Relative Increase (%)
NPO box (3–65 N; 120E–115 W)	1.22	1.30	+6.4
HNLC box (40–60 N; 170–135 W)	1.05	1.19	+13.4

change with changes in emissions of dust and other chemical species, and with changes in transport patterns.

4. Seasonal Variation of Dissolved Iron Fraction and Dissolved Iron Deposition Over the NPO Basin

[70] In previous sections, we focused on soluble iron formation during April 2001 due to the interest in dust sources, which are maximum in the spring, as well as the availability of observational data. However, it is important to evaluate the role of dust/pollution interactions in dissolved iron production over longer timescales, which is more relevant in terms of climatic impact. As an initial study toward this goal, we present the results of a one-year simulation performed for 2001. The results are presented in term of seasonal averages. However, since some of the winter months were used for the spin up of the model, winter season results are not displayed.

4.1. Average Concentrations and DIF Over the NPO

[71] Figure 11 displays the simulated seasonal distributions of dissolved iron and the associated dissolved iron fraction. As mentioned in previous sections, the total soluble iron is partly determined by initial condition on DIF (set to 0.45 %) and partly results from chemical processing during transport. These two contributions are displayed in Table 5 and Figure 12 for which seasonal concentrations have been averaged over the two north Pacific sub-region defined in section 3.2.4. In Table 5, we

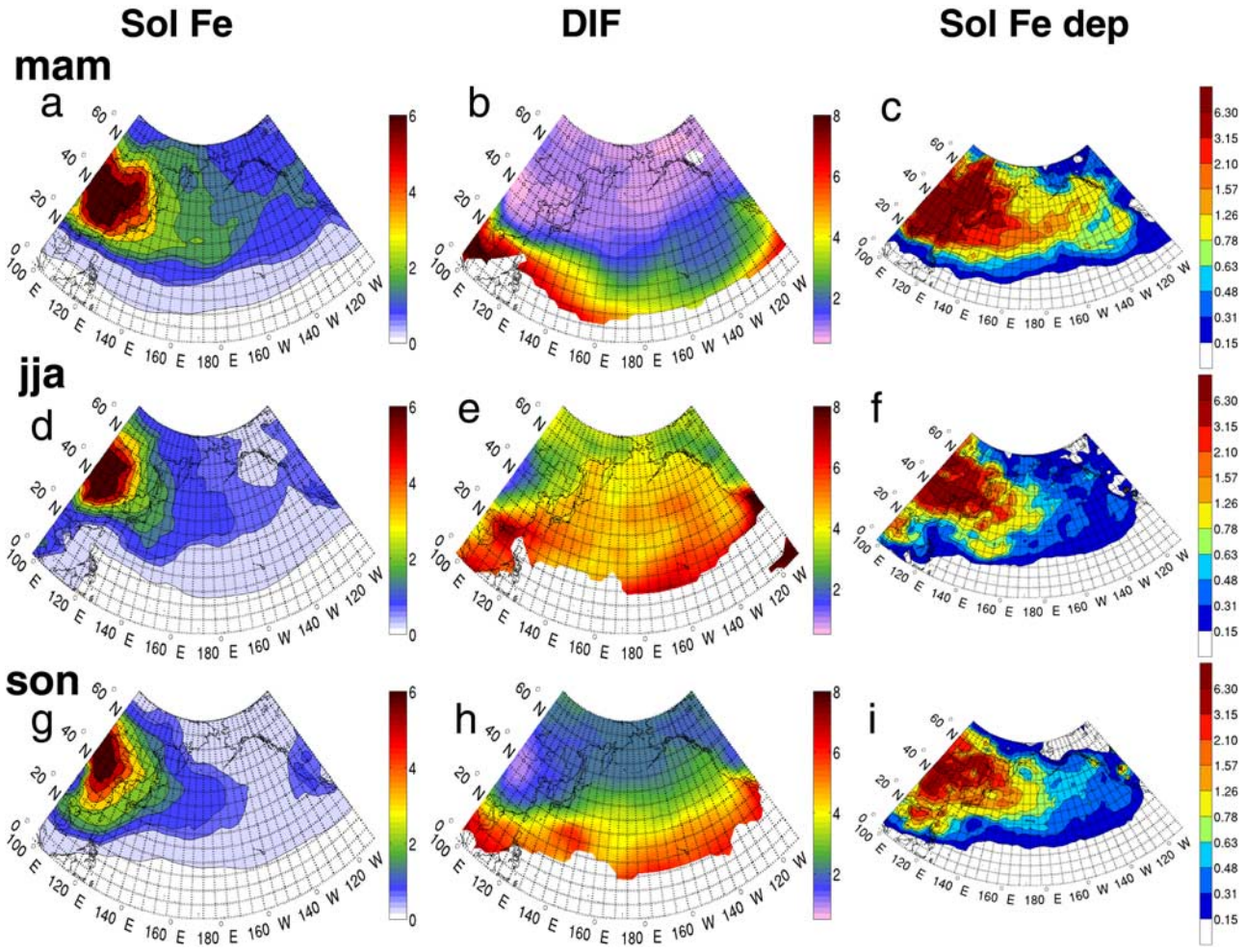

Figure 11. Vertically and seasonally averaged dust-soluble iron concentration, dust-dissolved iron fraction and soluble iron deposition for March, April, May (MAM), June, July, August (JJA), September, October, November (SON) of year 2001. (a, d, g) Simulated soluble iron concentration (ng m^{-3}). (b, e, h) Simulated dissolved iron fraction (in percent). Contours are plotted for dust-soluble iron concentrations exceeding 0.2 ng m^{-3}. (c, f, i) Simulated total deposition (mg m^{-2} a^{-1}).

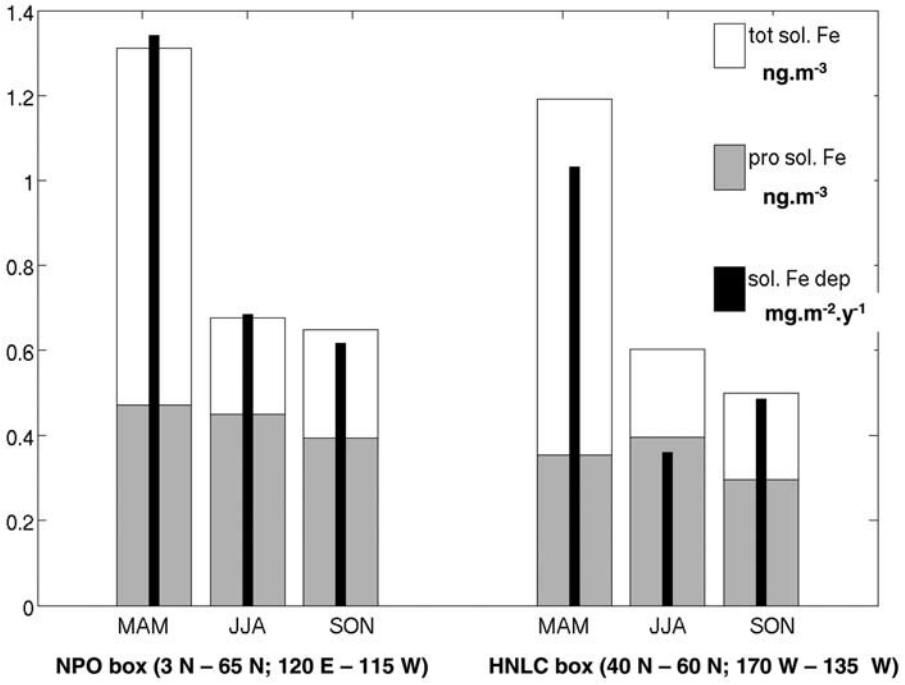

Figure 12. Seasonal soluble iron tropospheric concentration and surface deposition averaged over specific subregions (see also Figure 1). "pro. sol. Fe" stands for soluble iron formed by chemical processing and "tot. sol. Fe" for total soluble iron (see text).

report soluble iron concentrations calculated for initial DIF in the range between 0.05 and 1%, which corresponds to the range of DIF variability observed in the Dunuhang source region (as discussed in section 2).

[72] The maximum dissolved iron concentrations are obtained during the MAM spring period which corresponds to the maximum dust activity over east Asia. The seasonal DIF varies between 0.5 and 6% and tends to increase at the south of the domain and close to anthropogenic sources (Figure 11b), as a result of higher pollution/dust ratios and temperatures. In the spring, chemical processing accounts for about 36% (range 20 % to 83 % under different initial DIF conditions; see Table 5) of the total dissolved iron averaged over the north Pacific region and about 30% (range of 16 to 80 %) over the remote HNLC sub-region (Table 5 and Figure 12). The contribution of chemical processing to the production of dissolved iron in long-range transported aerosols is highest during the summertime (JJA) with values reaching ~66% (range of 47 to 95%) for both the NPO and HNLC regions (Table 5 and Figure 12). In summer, lower dust emissions and generally increased pollution concentrations, warmer temperatures, enhanced aerosol residence time due to less wet deposition and more stagnant conditions over the basin, are all factors which tend to enhance dissolved iron production. In the northern part of the domain DIF can now reach 4 to 6% which is larger than spring values (Figure 11e). In fall (SON), the simulated DIF tends to decrease compared to JJA, ranging from 2 to 6 % over the basin (Figure 11h). For SON, the average fraction of soluble iron formed via processing is about 60% (range of 40 to 93%, Table 5) in the NPO and remote HNLC sub-regions. Therefore pollution/dust interactions appear to be an important mechanism controlling the production of soluble iron during the less dusty summer and fall seasons.

4.2. Seasonal Deposition of Soluble Iron

[73] Dissolved iron deposition to the ocean surface is the most relevant quantity for evaluating biogeochemical impacts [*Jin et al.*, 2007; *Blain et al.*, 2008]. Deposition occurs via dry and wet deposition processes, both accounted for in GEOS-Chem. Figures 11c, 11f and 11i display the simulated seasonal average of soluble iron total (dry+wet) deposition. Consistent with most studies [*Mahowald et al.*, 2005; *Fan et al.*, 2006], dust dry deposition in GEOS-Chem is only significant in the neighborhood of intense continental dust sources whereas most of the deposition to the remote NPO (roughly East of 140 E) is dominated by wet removal (results not shown). On a yearly basis, the GEOS-Chem total dust deposition over the basin is very compa-

Table 5. Seasonal Average Soluble Iron Tropospheric Concentrations Calculated for NPO and HNLC Sub-Regions. "Tot. Sol. Fe" Represents Total Soluble Iron and "Pro. Sol. Fe" Represents the Contribution of Atmospheric Processing (in Percent)[a]

		NPO Box			HNLC Box		
DIF ini		MAM	JJA	SON	MAM	JJA	SON
0.05 %	Tot. sol. Fe (ng.m-3)	0.56	0.48	0.42	0.45	0.42	0.32
	Pro. sol. Fe (%)	83	95	94	80	95	93
0.45 %	Tot. sol. Fe (ng.m-3)	1.31	0.68	0.65	1.19	0.60	0.50
	Pro. sol. Fe (%)	36	66	60	30	65	60
1 %	Tot. sol. Fe (ng.m-3)	2.31	0.95	0.95	2.20	0.85	0.75
	Pro. sol. Fe (%)	20	47	41	16	46	40

[a]"DIF ini" represents the initial value of dissolved iron fraction at the dust source region (see text).

rable to the state of the art estimation of annual deposition fluxes published in the study by *Jickells et al.* [2005]. Seasonally, soluble iron deposition to the remote Pacific not only depends on total dust amount and atmospheric processing, as we have focused on thus far, but also on precipitation activity over the basin.

[74] Spring appears to be the most efficient season in terms of soluble iron deposition to the NPO and remote HNLC sub-regions (Figures 11c, 11f and 11i and Figure 12) compared to summer and fall. Relatively large concentrations of dissolved iron and greater amounts of precipitation occurring over the basin combine to give this spring maximum. Regionally, the spring deposition patterns displayed in Figures 11c and 12 show significant deposition levels in the northeastern Pacific region corresponding to the HNLC region.

[75] During summer and fall, simulated soluble iron deposition values are generally lower, particularly east of 180 E, including the northeastern Pacific region. For the HNLC sub-region, the average deposition is lower in summer than in fall despite the fact that mean soluble iron concentration evolve in the opposite direction (Figure 12). This difference is due to greater average rainfall occurring in fall over the HNLC sub-region.

[76] *Luo et al.* [2005] and *Fan et al.* [2006] have estimated the annual deposition fluxes of soluble iron by examining the possible influence of different processes, notably the effect of hematite dissolution, using a more simplified version of the M05 scheme. On an annual basis, our dissolved iron estimations are quite comparable in magnitude over the NPO. We obtain slightly larger values for the mean DIF and deposition flux over the basin, but these differences are small relative to uncertainties in iron cycle modeling and model to model variability. Another quantification of deposition fluxes has been proposed by *Fan et al.* [2006], including dust-SO_2 pollution interaction with a simplified two-step process. Over the NPO, our results show in general less iron processing and lower DIF values in remote regions. Our average soluble iron deposition fluxes are almost one order of magnitude lower than the estimates by *Fan et al.* [2006]. It is quite difficult to assess the reasons for discrepancies between models without carrying out detailed model intercomparison, which is beyond the scope of this study. One possible factor is that dust deposition is more intense in the study by *Fan et al.* [2006] since their global estimation is situated in the higher range compared to the *Jickells et al.* [2005] estimates. Another possible reason is that *Fan et al.* [2006] have used much faster mineral dissolution kinetics compared to our present scheme.

[77] If we consider a phytoplankton cellular Fe:C ratio of 5 μmol mol^{-1} [*Moore et al.*, 2002], we can very roughly estimate a primary production associated with iron deposition fluxes in the HNLC sub-region where iron likely serves as the limiting nutrient. Under this assumption and according to our results averaged for the nine simulation months during 2001, the primary production would be 2.4 molC m^{-2} yr^{-1} for this sub-region. If we assume now that pre-industrial DIF was constant and equal to 0.45 % (i.e., the initial value considered for unpolluted dust regions) this production would be reduced to 1.2 molC m^{-2} yr^{-1}. Therefore soluble iron derived from anthropogenic activities emission is responsible for roughly 50% of the primary production associated with iron deposition flux. This further suggests that anthropogenic factors should be represented in global biogeochemical models.

5. Conclusions

[78] Dissolution of iron contained in dust minerals during atmospheric transport is an important issue in order to understand and quantify the deposition of bioavailable iron to the ocean and ensuing biogeochemical impacts. In this study, we coupled a detailed iron dissolution scheme describing the effect of anthropogenic chemical compounds in the GEOS-Chem 3D chemistry transport scheme. Our conviction is that only a detailed treatment of complex chemistry processes occurring in the aerosol phase can allow for substantial improvement in understanding the observed variability in dissolved iron fraction. This study is a first step toward this goal.

[79] Heterogeneous chemistry occurring between coated dust particles and major anthropogenic gaseous species is very important because it regulates the pH of the coating solution forming on dust particles and the mineral dissolution kinetic and release of soluble iron. In the GEOS-Chem dust model we introduced mechanisms to account for the uptake of acidic trace gases and subsequent chemical reactions in deliquesced mineral aerosols. The simulated concentrations of major inorganic ions occurring in the dust mode were compared with different data sets over the Pacific Ocean. The model showed reasonable consistency with observations. Some problems have nevertheless been identified, the main one being a possible overestimation of solid gypsum formation which decreases the amount of sulfate in the solution and perturb its chemical composition and pH. The ionic strength of the solution might be therefore underestimated but further effect on pH and hematite dissolution rates are difficult to assess. Aerosol heterogeneous chemistry is an active research topic, and *Sullivan et al.* [2007] pointed out the complexity of dust/pollution interactions in the Asian outflow which remains a major challenge for current models.

[80] Focusing on the April 2001 period, different chemical environments occurring in the East Asia outflow have been studied with the model. In agreement with the box model study by *Meskhidze et al.* [2005] as well as soluble iron observations, we showed that iron dissolution rate is a function of dust-to-pollution ratio, and that medium dust/high pollution episodes were more efficient to produce soluble iron during transport over the remote Pacific.

[81] At the seasonal timescale, our simulations suggest that the largest production of soluble iron through chemical processing of dust occurs in summer, owing to higher pollution-to-dust ratios, enhanced temperature and longer residency time of particles over the NPO basin. However, because of frequent large dust outbreaks spring is still the period for the largest net export and deposition of dissolved iron to the Pacific. It should be noticed that chemical production rates of dissolved iron and the magnitude of bioavailable iron deposition to the ocean were calculated employing an initial composition of mineral dust and dissolved iron fraction representative of unpolluted source regions in the east Asia. Although these values were

determined from measurements, and were also discussed through a sensitivity study in M05, one should keep in mind that spatial variability of dust mineralogical composition is an important source of uncertainty in our model simulations. Since dust composition determines chemical properties (e.g., calcite buffering potential) of dust particles, before extending this study to the globe, the dust mineral composition variability should be explicitly accounted for.

[82] Simulated DIF fields were also in reasonable agreement with the few observations available over our domain. However, over Kosan site, we saw that anthropogenic dissolved iron emitted as a result of combustion activities could be locally important and explain the discrepancy between model and measured soluble iron concentrations. As suggested by the recent *Luo et al.* [2008] study, these sources should be considered in regional and global iron modeling. Although actually not well understood and constrained, the treatment of anthropogenic mode iron processing could follow some similar path to dust mode processing, since acidity of particles is an essential factor to determine iron dissolution.

[83] To the extent that this mobilized Fe is the limiting micronutrient in oceanic ecosystems, air pollution from China could be responsible for enhancing the marine ecosystem productivity associated to iron deposition (and perhaps carbon uptake) in North Pacific Ocean waters. Rough estimates showed that this enhancement could reach 50% in a remote HNLC region, with an iron induced primary production increasing from a pre-industrial values of 1.25 molC m^{-2} yr^{-1} to 2.44 molC m^{-2} yr^{-1}. This result (originally proposed by *Meskhidze et al.* [2003]) could be important for understanding and predicting the climate change and requires further investigations, involving more detailed observations and modeling studies of the interactions between airborne dust and air-pollutants. Sensitivity simulations for doubling of SO_2 emissions showed that production of dissolved iron in mineral dust could increase by up to 40% in the remote Pacific region, primarily due to increased acidity.

[84] Simulated dissolved iron fractions obtained in this study range from 0.5 to 8 %. Note that this domain is likely to be a favorable location for strong dust-pollution interactions. These values are within the range of measurements conducted in North Pacific [*Luo et al.*, 2005; *Chen*, 2005], although at the global scale much larger DIF are sometimes reported in literature. In addition to uncertainties associated with dust emission, transport, composition and heterogeneous chemistry, acid mobilization mechanisms in deliquesced aerosols could also be the subject of further improvement [*Cwiertny et al.*, 2008]. Furthermore, in this study we primarily focused on acid mobilization of iron in deliquesced aerosol and did not explicitly consider enhancement of iron dissolution rates by photo-reductive dissolution in the presence of organic complexing agents [*Cornell and Schindler*, 1987; *Suter et al.*, 1988; *Siffert and Sulzberger*, 1991; *Pehkonen et al.*, 1993] or clouds [*Spokes et al.*, 1994; *Desboeufs et al.*, 2003; *Spokes and Jickells*, 1996; *Hand et al.*, 2004; *Mackie et al.*, 2005]. Despite the great advancement in our capability of modeling enhancement of iron dissolution by organic compounds like oxalate, the mechanistic treatment of dissolution and photo-chemical cycling of iron in regional and global atmospheric chemistry-transport models remains as a challenging issue. Toward this goal, it is necessary to use the models able to concurrently treat the organic precursor chemistry, aerosol thermodynamics and aqueous chemistry, and reductive photo-dissolution of iron oxides. Several additional improvements to iron dissolution scheme could include more complete thermodynamic equilibrium (ISORROPIA II) and aerosol microphysics schemes [*Trivitayanurak et al.*, 2007].

[85] **Acknowledgments.** We would like to acknowledge the Harvard GEOS-Chem team for providing model, data support and excellent documentation. We also would like to thank the two anonymous reviewers for their constructive critics.

References

Achilles, K. M., T. M. Church, S. W. Wilhelm, G. W. Luther, and D. A. Hutchins (2003), Bioavailability of iron to Trichodesmium colonies in the western subtropical Atlantic Ocean, *Limnol. Oceanogr.*, *48*(6), 2250–2255.

Alexander, B., R. J. Park, D. J. Jacob, Q. B. Li, R. M. Yantosca, J. Savarino, C. C. W. Lee, and M. H. Thiemens (2005), Sulfate formation in sea-salt aerosols: Constraints from oxygen isotopes, *J. Geophys. Res.*, *110*, D10307, doi:10.1029/2004JD005659.

Archer, D. E., and K. Johnson (2000), A model of the iron cycle in the ocean, *Global Biogeochem. Cycles*, *14*(1), 269–279.

Arimoto, R., et al. (2006), Characterization of Asian dust during ACE-Asia, *Global Planet. Change*, *52*, 23–56.

Aumont, O., L. Bopp, and M. Schulz (2008), What does temporal variability in aeolian dust deposition contribute to sea-surface iron and chlorophyll distributions?, *Geophys. Res. Lett.*, *35*, L07607, doi:10.1029/2007GL031131.

Azuma, K., and H. Kametani (1964), Kinetics of dissolution of ferric oxide, *Trans. Metall. Soc. AIME*, *230*, 853–862.

Baker, A. R., M. French, and K. L. Linge (2006), Trends in aerosol nutrient solubility along a west-east transect of the Saharan dust plume, *Geophys. Res. Lett.*, *33*, L07805, doi:10.1029/2005GL024764.

Bey, I., D. J. Jacob, R. M. Yantosca, J. A. Logan, B. Field, A. M. Fiore, Q. Li, H. Liu, L. J. Mickley, and M. Schultz (2001a), Global modeling of tropospheric chemistry with assimilated meteorology: Model description and evaluation, *J. Geophys. Res.*, *106*(D19), 23,073–23,095.

Bey, I., D. J. Jacob, J. A. Logan, and R. M. Yantosca (2001b), Asian chemical outflow to the Pacific in spring: Origins, pathways, and budgets, *J. Geophys. Res.*, *106*(D19), 23,097–23,113.

Blain, S., et al. (2007), Effect of natural iron fertilization on carbon sequestration in the Southern Ocean, *Nature*, *446*, doi:10.1038/nature05700.

Blain, S., S. Bonnet, and C. Guieu (2008), Dissolved iron distribution in the tropical and sub tropical South Eastern Pacific, *Biogeosciences*, *5*, 269–280.

Böke, H., et al. (1999), Effect of airborne particles on SO_2-calcite reaction, *Appl. Surf. Sci.*, *140*, 70–82.

Bonnet, S., and C. Guieu (2004), Dissolution of atmospheric iron in seawater, *Geophys. Res. Lett.*, *31*, L03303, doi:10.1029/2003GL018423.

Boyle, E. A., B. Bergquist, and R. Kayser (2005), Iron, manganese and lead at Hawaii Ocean Timeseries Station ALOHA: Temporal variability and intermediate water hydrothermal plume, *Geochem. Cosmochim. Acta*, *69*, 933–952.

Carmichael, G. R., et al. (2001), Model intercomparison study of long range transport and sulfur deposition in East Asia (MICS-Asia), *Water Air Soil Pollut.*, *130*, 51–62.

Cassar, N., et al. (2007), The Southern Ocean biological response to aeolian iron deposition, *Science*, *317*, 1067, doi:10.1126/science.1144602.

Chen, Y. (2005), Sources and fate of atmospheric nutrients over the remote oceans and their role on controlling marine diazotrophic microorganisms, thesis, Univ. of Maryland, College Park, Md.

Chuang, P. Y., R. M. Duvall, M. M. Shafer, and J. J. Schauer (2005), The origin of water soluble particulate iron in the Asian atmospheric outflow, *Geophys. Res. Lett.*, *32*, L07813, doi:10.1029/2004GL021946.

Coey, J. M. D. (1988), Magnetic properties of iron in soil iron oxides and clay minerals, in *Iron in Soils and Clay Minerals*, *NATO ASI Ser.*, vol. 217, edited by J. W. Stucki, B. A. Goodman, and U. Schwertmann, Springer, New York.

Cornell, R. M., and P. W. Schindler (1987), Photochemical dissolution of goethite in acid oxalate solution, *Clay Miner.*, *35*, 347–352.

Cwiertny, D. M., J. Baltrusaitis, G. J. Hunter, A. Laskin, M. M. Scherer, and V. H. Grassian (2008), Characterization and acid-mobilization study of iron-containing mineral dust source materials, *J. Geophys. Res.*, *113*, D05202, doi:10.1029/2007JD009332.

Desboeufs, K. V., R. Losno, and J. L. Colin (2001), Factors influencing aerosol solubility during cloud processes, *Atmos. Environ.*, *35*(20), 3529–3537.

Desboeufs, K. V., R. Losno, and J. L. Colin (2003), Relationship between droplet pH and aerosol dissolution kinetics: Effect of incorporated aerosol particles on droplet pH during cloud processing, *J. Atmos. Chem.*, *46*, 159–172.

Duce, R. A., and N. W. Tindale (1991), Atmospheric transport of iron and its deposition in the ocean, *Limnol. Oceanogr.*, *36*(8), 1715–1726.

Fairlie, D. T., D. J. Jacob, and R. J. Park (2007), The impact of transpacific transport of mineral dust in the United States, *Atmos. Environ.*, *41*, 1251–1266.

Fan, S.-M., W. J. Moxim, and H. Levy II (2006), Aeolian input of bioavailable iron to the ocean, *Geophys. Res. Lett.*, *33*, L07602, doi:10.1029/2005GL024852.

Fountoukis, C., and A. Nenes (2007), ISORROPIA II: A computationally efficient aerosol thermodynamic equilibrium model for K+, Ca2+, Mg2+, NH4+, Na+, SO42−, NO3−, Cl−, H2O aerosols, *Atmos. Chem. Phys.*, *7*, 4639–4659.

Fung, I., S. K. Meyn, I. Tegen, S. Doney, J. John, and J. Bishop (2000), Iron supply and demand in the upper ocean, *Global Biogeochem. Cycles*, *14*, 281–295.

Gao, Y., S. Fan, and J. L. Sarmiento (2003), Aeolian iron input to the ocean through precipitation scavenging: A modeling perspective and its implication for natural iron fertilization in the ocean, *J. Geophys. Res.*, *108*(D7), 4221, doi:10.1029/2002JD002420.

Gorichev, I. G., S. G. Ashkharua, S. K. Vainman, and N. G. Klyuchnikov (1976), The applicability of the topochemical model to the dissolution of certain oxides in acids, *Russ. J. Phys. Chem.*, *50*(6), 975–976.

Hand, J. L., N. M. Mahowald, Y. Chen, R. L. Siefert, C. Luo, A. Subramaniam, and I. Fung (2004), Estimates of atmospheric-processed soluble iron from observations and a global mineral aerosol model: Biogeochemical implications, *J. Geophys. Res.*, *109*, D17205, doi:10.1029/2004JD004574.

Heald, C. L., D. J. Jacob, R. J. Park, B. Alexander, T. D. Fairlie, D. A. Chu, and R. M. Yantosca (2006a), TransPacific transport of Asian anthropogenic aerosols and its impact on surface air quality in the United States, *J. Geophys. Res.*, *111*, D14310, doi:10.1029/2005JD006847.

Heald, C. L., et al. (2006b), Concentrations and sources of organic carbon aerosol in the free troposphere over north America, *J. Geophys. Res.*, *111*, D23S47, doi:10.1029/2006JD007705.

Herring, J. A., R. J. Ferek, and P. V. Hobbs (1996), Heterogeneous chemistry in the smoke plume from the 1991 Kuwait oil fires, *J. Geophys. Res.*, *101*(D9), 14,451–14,463.

Huebert, B. J., et al. (2003), An overview of ACE-Asia: Strategies for quantifying the relationships between Asian aerosols and their climatic impacts, *J. Geophys. Res.*, *108*(D23), 8633, doi:10.1029/2003JD003550.

Jacob, D. J., J. H. Crawford, M. M. Kleb, V. S. Connors, R. J. Bendura, J. L. Raper, G. W. Sachse, J. C. Gille, L. Emmons, and C. L. Heald (2003), Transport and Chemical Evolution over the Pacific (TRACE-P) aircraft mission: Design, execution, and first results, *J. Geophys. Res.*, *108*(D20), 9000, doi:10.1029/2002JD003276.

Jickells, T. D., et al. (2005), Global iron connections between desert dust, ocean biogeochemistry, and climate, *Science*, *308*, 67–71.

Jin, X., N. Gruber, H. Frenzel, S. C. Doney, and J. C. McWilliams (2007), The impact on atmospheric CO_2 of iron fertilization induced changes in the ocean's biological pump, *Biogeosci. Discuss.*, *4*, 3863–3911.

Jordan, C. E., J. E. Dibb, B. E. Anderson, and H. E. Fuelberg (2003), Uptake of nitrate and sulfate on dust aerosols during TRACE-P, *J. Geophys. Res.*, *108*(D21), 8817, doi:10.1029/2002JD003101.

Journet, E., K. V. Desboeufs, S. Caquineau, and J.-L. Colin (2008), Mineralogy as a critical factor of dust iron solubility, *Geophys. Res. Lett.*, *35*, L07805, doi:10.1029/2007GL031589.

Kim, B. G., and S. U. Park (2001), Transport and evolution of a wintertime Yellow sand observed in Korea, *Atmos. Environ.*, *35*(18), 3191–3201.

Kim, S. W., S. C. Yoon, J. Kim, and S. Y. Kim (2007), Seasonal and monthly variations of columnar aerosol optical properties over East Asia determined from multi-year MODIS, LIDAR, and AERONET Sun/sky radiometer measurements, *Atmos. Environ.*, *41*, 1634–1651.

Kline, J., et al. (2004), Aerosol composition and size versus altitude measured from the C-130 during ACE-Asia, *J. Geophys. Res.*, *109*, D19S08, doi:10.1029/2004JD004540.

Liu, H., D. J. Jacob, I. Bey, and R. M. Yantosca (2001), Constraints from ^{210}Pb and ^{7}Be on wet deposition and transporting a global three-dimensional chemical tracer model driven by assimilated meteorological fields, *J. Geophys. Res.*, *106*, 12,109–12,128.

Luo, C., N. M. Mahowald, N. Meskhidze, Y. Chen, R. L. Siefert, A. R. Baker, and A. M. Johansen (2005), Estimation of iron solubility from observations and a global aerosol model, *J. Geophys. Res.*, *110*, D23307, doi:10.1029/2005JD006059.

Luo, C., N. Mahowald, T. Bond, P. Y. Chuang, P. Artaxo, R. Siefert, Y. Chen, and J. Schauer (2008), Combustion iron distribution and deposition, *Global Biogeochem. Cycles*, *22*, GB1012, doi:10.1029/2007GB002964.

Mackie, D. S., P. W. Boyd, K. A. Hunter, and G. H. McTainsh (2005), Simulating the cloud processing of iron in Australian dust: pH and dust concentration, *Geophys. Res. Lett.*, *32*, L06809, doi:10.1029/2004GL022122.

Mahowald, N. M., A. R. Baker, G. Bergametti, N. Brooks, R. A. Duce, T. D. Jickells, N. Kubilay, J. M. Prospero, and I. Tegen (2005), Atmospheric global dust cycle and iron inputs to the ocean, *Global Biogeochem. Cycles*, *19*, GB4025, doi:10.1029/2004GB002402.

Martin, J. H. (1990), Glacial-interglacial CO_2 change: The iron hypothesis, *Paleoceanography*, *5*(1), 1–13.

Meskhidze, N., W. L. Chameides, A. Nenes, and G. Chen (2003), Iron mobilization in mineral dust: Can anthropogenic SO_2 emissions affect ocean productivity?, *Geophys. Res. Lett.*, *30*(21), 2085, doi:10.1029/2003GL018035.

Meskhidze, N., W. L. Chameides, and A. Nenes (2005), Dust and pollution: A recipe for enhanced ocean fertilization?, *J. Geophys. Res.*, *110*, D03301, doi:10.1029/2004JD005082.

Meskhidze, N., A. Nenes, W. L. Chameides, C. Luo, and N. Mahowald (2007), Atlantic Southern Ocean productivity: Fertilization from above or below?, *Global Biogeochem. Cycles*, *21*, GB2006, doi:10.1029/2006GB002711.

Moore, J. K., S. C. Doney, D. M. Glover, and I. Y. Fung (2002), Iron cycling and nutrient limitation patterns in surface waters of the world ocean, *Deep Sea Res., Part II*, *49*, 463–508.

Mori, I., M. Nishikawa, and Y. Iwasaka (1998), Chemical reaction during the coagulation of ammonium sulphate and mineral particles in the atmosphere, *Sci. Total Environ.*, *224*, 1–3.

Nakicenovic, N., et al. (2000), *Special Report on Emissions Scenarios: A Special Report of Working Group III of the Intergovernmental Panel on Climate Change*, 599 pp., Cambridge Univ. Press, Cambridge, U.K. (Available at http://www.grida.no/climate/ipcc/emission/index.htm)

Nenes, A., S. N. Pandis, and C. Pilinis (1998), ISORROPIA: A new thermodynamic equilibrium model for multiphase multicomponent inorganic aerosols, *Aquat. Geochem.*, *4*(1), 123–152.

Ohara, T., H. Akimoto, J. Kurokawa, N. Horii, K. Yamaji, X. Yan, and T. Hayasaka (2007), An Asian emission inventory of anthropogenic emission sources for the period 1980–2020, *Atmos. Chem. Phys.*, *7*, 4419–4444.

Park, R. J., D. J. Jacob, B. D. Field, R. M. Yantosca, and M. Chin (2004), Natural and transboundary pollution influences on sulfate-nitrate-ammonium aerosols in the United States: Implications for policy, *J. Geophys. Res.*, *109*, D15204, doi:10.1029/2003JD004473.

Pehkonen, S. O., R. Siefert, Y. Erel, S. Webb, and M. R. Hoffmann (1993), Photoreduction of iron oxyhydroxides in the presence of important atmospheric organic compounds, *Environ. Sci. Technol.*, *27*, 2056–2062.

Prospero, J. M., D. L. Savoie, and R. Arimoto (2003), Long-term record of nss-sulfate and nitrate in aerosols on Midway Island, 1981–2000: Evidence of increased (now decreasing?) anthropogenic emissions from Asia, *J. Geophys. Res.*, *108*(D1), 4019, doi:10.1029/2001JD001524.

Sarthou, G., et al. (2003), Atmospheric iron deposition and sea-surface dissolved iron concentrations in the East Atlantic, *Deep Sea Res., Part I*, *50*(10–11), 1339–1352.

Siefert, R. L., S. O. Pehkonen, Y. Erel, and M. R. Hoffmann (1994), Iron photochemistry of aqueous suspensions of ambient aerosol with added organic acids, *Geochim. Cosmochim. Acta*, *58*(15), 3271–3279.

Siffert, C., and B. Sulzberger (1991), Light-induced dissolution of hematite in the presence of oxalate: A case study, *Langmuir*, *7*(8), 1627–1634.

Song, C. H., and G. R. Carmichael (2001), A three-dimensional modelling investigation of the evolution processes of dust and sea-salt particles in east Asia, *J. Geophys. Res.*, *106*(D16), 18,131–18,154.

Spokes, L., and T. D. Jickells (1996), Factors controlling the solubility of aerosol trace metals in the atmosphere and on mixing into seawater, *Aquat. Chem.*, *1*, 355–374.

Spokes, L. J., T. D. Jickells, and B. Lim (1994), Solubilization of aerosol trace metals by cloud processing: A laboratory study, *Geochim. Cosmochim. Acta*, *58*, 3281–3287.

Sullivan, R. C., S. A. Guazzotti, D. A. Sodeman, and K. A. Prather (2007), Direct observations of the atmospheric processing of Asian mineral dust, *Atmos. Chem. Phys.*, *7*, 1213–1236.

Suter, D., C. Siffert, B. Sulzberger, and W. Stumm (1988), Catalytic dissolution of Iron(III)(hydr)oxides by oxalic acid in the presence of Fe(II), *Naturwissenschaften*, *75*, 571–573.

Trivitayanurak, W., P. J. Adams, D. V. Spracklen, and K. S. Carslaw (2007), Tropospheric aerosol microphysics simulation with assimilated meteorology: Model description and intermodel comparison, *Atmos. Chem. Phys. Discuss.*, *7*, 14369–14411.

Warneck, P. (2000), *Chemistry of the Natural Atmosphere*, Academic, San Diego, Calif.

Zhang, Y., and G. R. Carmichael (1999), The role of mineral aerosol in tropospheric chemistry in east Asia—A model study, *J. Appl. Meteorol.*, *38*, 353–366.

Zhou, G., and K. Tazaki (1996), Seasonal variation of gypsum in aerosol and its effect on the acidity of wet precipitation on the Japan Sea side of Japan, *Atmos. Environ.*, *30*(19), 3301–3308.

Zhu, X., J. M. Prospero, D. L. Savoie, F. J. Millero, R. G. Zika, and E. S. Saltzman (1993), Photoreduction of iron (III) in marine mineral aerosol solutions, *J. Geophys. Res.*, *98*(D5), 9039–9046.

Zhuang, G., Z. Yi, R. A. Duce, and P. R. Brown (1992), Link between iron and sulphur cycles suggested by detection of Fe(II) in remote marine aerosols, *Nature*, *355*, 537–539.

Y. Chen, Trinity Consultants, 1 Technology Drive, Suite F215, Irvine, CA 92618, USA.

P. Y. Chuang, Earth and Planetary Sciences Department, University of California, Earth and Marine Science Building, Santa Cruz, CA 95064, USA.

N. Meskhidze, Department of Marine, Earth and Atmospheric Sciences, North Carolina State University, 2800 Faucette Drive, Rm. 1125 Jordan Hall, Raleigh, NC 27695-8208, USA.

F. Solmon, Laboratoire d'Aérologie, UPS-CNRS, 14 avenue Edouard Belin, F-31400 Toulouse, France. (solf@aero.obs-mip.fr)